Acid-in-Clay Electrolyte for Wide-Temperature-Range and Long-Cycle Proton Batteries

Shitong Wang, Heng Jiang, Yanhao Dong, David Clarkson, He Zhu, Charles M. Settens, Yang Ren, Thanh Nguyen, Fei Han, Weiwei Fan, So Yeon Kim, Jianan Zhang, Weijiang Xue, Sean K. Sandstrom, Guiyin Xu, Emre Tekoglu, Mingda Li, Sili Deng, Qi Liu, Steven G. Greenbaum, Xiulei Ji,* Tao Gao,* and Ju Li*

Proton conduction underlies many important electrochemical technologies. A family of new proton electrolytes is reported: acid-in-clay electrolyte (AiCE) prepared by integrating fast proton carriers in a natural phyllosilicate clay network, which can be made into thin-film (tens of micrometers) fluid-impervious membranes. The chosen example systems (sepiolite–phosphoric acid) rank top among the solid proton conductors in terms of proton conductivities (15 mS cm^{-1} at 25 °C, 0.023 mS cm^{-1} at −82 °C), electrochemical stability window (3.35 V), and reduced chemical reactivity. A proton battery is assembled using AiCE as the solid electrolyte membrane. Benefitting from the wider electrochemical stability window, reduced corrosivity, and excellent ionic selectivity of AiCE, the two main problems (gassing and cyclability) of proton batteries are successfully solved. This work draws attention to the element cross-over problem in proton batteries and the generic "acid-in-clay" solid electrolyte approach with superfast proton transport, outstanding selectivity, and improved stability for room- to cryogenic-temperature protonic applications.

1. Introduction

An electrolyte conducts specific ions between two electrodes in electrochemical devices while forbidding electrons and other unintended ions to cross. The electrolyte/separator combination should also have sufficient mechanical strength and toughness to prevent two electrodes from mechanical penetration, and ideally can also be made thin enough (10^1 μm) to save space and weight. Its properties set the boundaries for the performance of electrochemical cells, such as power density, energy density, and durability.[1] Among the various solid electrolytes, the ones that conduct alkali metal ions (especially for Li$^+$) are extensively developed for rechargeable batteries.[2] The developments of lead-acid batteries and hydrogen fuel cells over the past century have demonstrated

S. Wang, Y. Dong, T. Nguyen, F. Han, W. Fan, W. Xue, G. Xu, E. Tekoglu, M. Li, J. Li
Department of Nuclear Science and Engineering
Massachusetts Institute of Technology
Cambridge, MA 02139, USA
E-mail: liju@mit.edu
S. Wang, T. Gao
Department of Chemical Engineering
The University of Utah
Salt Lake City, UT 84112, USA
E-mail: taogao@chemeng.utah.edu
H. Jiang, S. K. Sandstrom, X. Ji
Department of Chemistry
Oregon State University
Corvallis, OR 97331, USA
E-mail: david.ji@oregonstate.edu

The ORCID identification number(s) for the author(s) of this article can be found under https://doi.org/10.1002/adma.202202063.

D. Clarkson, S. G. Greenbaum
Department of Physics and Astronomy
Hunter College
City University of New York
New York, NY 10065, USA
H. Zhu, Y. Ren, Q. Liu
Department of Physics
City University of Hong Kong
Kowloon, Hong Kong 999077, China
C. M. Settens
Materials Research Laboratory
Massachusetts Institute of Technology
Cambridge, MA 02139, USA
S. Y. Kim, J. Li
Department of Materials Science and Engineering
Massachusetts Institute of Technology
Cambridge, MA 02139, USA
J. Zhang, S. Deng
Department of Mechanical Engineering
Massachusetts Institute of Technology
Cambridge, MA 02139, USA

**ADVANCED
SCIENCE NEWS**

www.advancedsciencenews.com
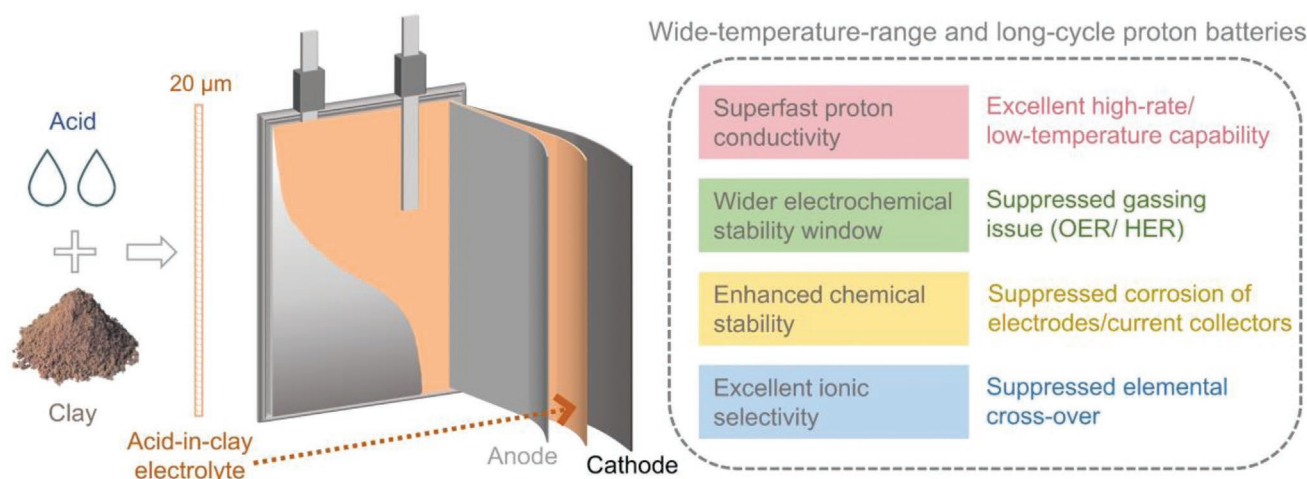
**ADVANCED
MATERIALS**

www.advmat.de

Figure 1. Schematic diagram of acid-in-clay electrolytes and their advantages for wide-temperature-range and long-cycle proton batteries.

the success of protons in energy storage and conversion.[3] Recently, there has been a renewed interest in proton batteries;[4] however, the development of high-performance proton batteries is hindered by the gassing problem and the poor cycle life.[5] Due to the narrow electrochemical stability window of bulk liquid water (1.23 V), hydrogen evolution reaction (HER) and oxygen evolution reaction (OER) can be easily triggered in aqueous electrolytes, which restrict the operating voltage of proton batteries and lead to severe gassing problems.[6] The gassing will expand the pouch cell, degrade the volumetric energy density at the battery pack level, and cause safety problems. Attached gas bubbles also reduce the true contact area between the current collector and electrolyte, increase impedance, and accelerate degradation. In addition, the acidic electrolytes can cause the dissolution of the current collectors or electrode materials.[5] Several strategies have been proposed to address these challenges. One strategy is to broaden the voltage window by coupling an alkaline electrolyte with an acidic one.[7] Such a design separates the acidic electrolyte from the alkaline electrolyte by using multiple cell compartments, adding extra weight and volume. Alternatively, new proton electrolytes are being investigated. Nonaqueous electrolytes based on aprotic solvents are attractive due to their noncorrosive nature and wide electrochemical stability windows,[8] but they are limited by the flammability and high cost. Another notable example of the new electrolyte is the water-in-salt electrolytes, in which the stability window can be expanded by increasing the molar ratio of salt/water.[9] Yet, the high viscosity and low ionic conductivity remain a problem. Hitherto, none of these strategies have fully addressed the challenges of rechargeable proton batteries, and few studies examine the element cross-over problem, a crucial contributor to capacity fading of the full cell.

A solid electrolyte may widen the electrochemical stability window, suppress the dissolution of current collectors/active materials, and prevent side reaction/cross-over of unwanted ions. Nafion is the most well-known solid proton electrolyte, but its fast proton conductivity (10^2–10^3 mS cm^{-1}) can only be maintained at a fully hydrated state (Table S1, Supporting Information). Polybenzimidazole (PBI), heteropoly acids (HPA), layered hydrates, metal–organic frameworks (MOF), and covalent

organic frameworks (COF) are also well-developed solid proton conductors (Table S1, Supporting Information). However, their proton conductivity is not satisfactory at/below room temperature (10^{-4} to 10 mS cm^{-1}, inset in Figure 2a). Recently, modified PBI, HPA, and polymers with good proton conductivities have been developed, but most are used in high humidity environments for fuel cells (Table S1, Supporting Information). For the above solid electrolytes, which rely on the thermal fluctuation of water molecules (protons mainly transport via the structural diffusion mechanism[10]), the proton conductivity drops dramatically when humidity or temperature decreases. Additionally, the poor thermodynamic stability of water limits their working voltage, and conduction of other cations is possible because of the high-water content in the electrolytes, resulting in low proton-transport selectivity.

Natural clays contain abundant hydrophilic groups on the internal surfaces, which can anchor proton donors, such as H_2O, acids, or alkalis, by hydrogen bonds or even covalent bonds.[11] The formed composites, also called geopolymers, have been widely used as binders, adsorbents, pH buffering agents, and catalysts.[12] However, few composites have been regarded as solid electrolytes for proton batteries. In this work, we introduce a series of inorganic solid proton electrolytes, denoted as acid-in-clay electrolytes (AiCEs), that will address the gassing, corrosion, and element cross-over problems of proton batteries. AiCEs are synthesized by absorbing H_3PO_4 into phyllosilicate clays to form gel-like all-inorganic materials (**Figure 1**). Compared with liquid H_3PO_4 electrolytes, these AiCEs demonstrate superfast proton conductivities (similar to aqueous electrolytes but extended to liquid-nitrogen temperature without phase transition), wider electrochemical stability windows (suppressing gassing), enhanced chemical stability (inhibiting corrosion of electrodes/current collectors), and excellent ionic selectivity (restricting unwanted element cross-over). As a result, the all-solid proton batteries with AiCEs show excellent proton-transport characteristics (33% capacity retention at 720 C under room temperature and 42% capacity retention at 1 C under −60 °C) and cycling performance (20 000 stable cycles at 50 C under room temperature and 3000 stable cycles at 3 C under −20 °C).

**ADVANCED
SCIENCE NEWS**

www.advancedsciencenews.com

**ADVANCED
MATERIALS**

www.advmat.de

2. Results

2.1. AiCE Synthesis and Proton-Transport Properties

Based on the ratio of tetrahedra sheets and octahedral sheets in the phyllosilicate network, clay minerals can be classified as 1:1 type (i.e., halloysite) and 2:1 type (i.e., bentonite, sepiolite)[13] (Figure S1, Supporting Information). In this paper, sepiolite is chosen as the first example system for fabricating AiCE and proton batteries due to its large internal surface area (Figure S2a, Supporting Information).[14] Afterward, the AiCE approach is further demonstrated with another two representative clays (bentonite and halloysite), and another representative acid (sulfuric acid). Thermogravimetric analysis (TGA, Figure S2b, Supporting Information) shows that the sepiolite contains 8.7 wt% adsorbed water and 7.5 wt% structural water, based on which its chemical formula can be written as $Mg_2H_2(SiO_3)_3 \cdot 3.0H_2O$. The dry clay powder is not malleable enough to make a solid electrolyte. In contrast, the sepiolite becomes a gel-like solid when a certain amount of water (weight ratio of water:clay = 3:1) is absorbed (Table S2, Supporting Information) and shows a proton conductivity of $\sigma = 0.18$ mS cm^{-1} at 25 °C. This finding confirms that the absorbed proton donor can render the clay proton-conductivity despite the low conductivity. Since liquid phosphoric acid has the highest proton conductivity among all known pure substances,[15] the question is whether the proton conductivity of the sepiolite can be further enhanced if phosphoric acid is integrated into the clay.

To address this question, a series of samples were made by mixing phosphoric acid with sepiolite clay powders. The proton concentration was tuned by changing the molar ratio (R) of acid molecules to water in the acid solution, together with the liquid (the acid solution) to solid (clay powder) weight ratio (N) (Table S2, Supporting Information). R was adjusted from 0 to ≈1.0 (85 wt% H_3PO_4), and N was adjusted in the range of 1–6. We found when N is small the AiC compounds are too dry for AiC particles to bind with each other, but when N is large the AiC compounds become fluid-like. The ionic conductivities of these samples were measured (**Table 1** and Figure S3a and Table S1, Supporting Information), and the maximum values of 15 mS cm^{-1} at 25 °C and 0.023 mS cm^{-1} at −82 °C were obtained when $R = 0.3$ and $N = 4$ (hereinafter denoted as SP-0.3-4, in which S stand for sepiolite and P stands for phosphoric acid). The molar formula of SP-0.3-4 can be written as $Mg_2Si_3O_7(OH)_2 \cdot 34.0H_2O \cdot 10.0H_3PO_4$ (the schematic diagram

of the empirical reaction between the acid and clay is illustrated in Figure S4, Supporting Information). The activation energy is calculated by fitting the results with the Arrhenius equation (Figure S3c, Supporting Information). Surprisingly, in the range of 25 to −20 °C, the effective activation energy is lower than most of the best proton electrolytes, including fully hydrated Nafion and liquid H_3PO_4, as well as most conductive solid Li-ion electrolytes (Table 1). In comparison, H_3PO_4 solutions show a maximum conductivity at $R = 0.3$ (63 wt% of H_3PO_4, denoted as H_3PO_4-0.3) (Table S3, Figure S3b, Supporting Information). The activation energy of SP-0.3-4 is slightly lower than that of H_3PO_4-0.3 (Table 1 and Table S4, Supporting Information), suggesting a reduced barrier for proton conduction in the AiCE. ^1H solid-state NMR spectroscopy further confirms the fast proton transport in AiCE with an apparent activation energy of 0.15 eV above 0 °C (Figure S5a,b, Supporting Information). The calculated diffusion coefficients from NMR are 1.4×10^{-11} m^2 s^{-1} at 25 °C and 2.1×10^{-12} m^2 s^{-1} at −40 °C (Figure S5c,d, Supporting Information), which are comparable to those of liquid H_3PO_4.[16] It should be noted that the equivalent concentration of acid (H_3PO_4) in SP-0.3-4 is 8.6 mol L^{-1}, which is close to the 9.5 mol L^{-1} concentration of the concentrated acid (H_3PO_4-0.3). This similarity in acid concentration suggests that the packed-acid mechanism[10] could be operative for AiCE. Compared with the structural diffusion mechanism (the main proton-transport mechanism in dilute acids or solid electrolytes that relies on humidity), the packed-acid mechanism (the proton-transport mechanism in concentrated acids or AiCEs) will weaken H-bonds, resulting in enhanced proton transport.[10a] The comparison between the structural diffusion mechanism and the packed-acid mechanism is illustrated in Figure S6, Supporting Information. Compared with the recently reported solid proton electrolytes[17] and liquid proton electrolytes, the AiCE's proton conductivity is among the best (**Figure 2**a).

To examine the electrochemical and chemical stability windows of the electrolyte, linear scanning voltammetry is first performed (Figure 2b). For SP-0.3-4, HER starts at −1.25 V, and OER starts at ≈2.1 V (vs Pt^{2+}/Pt), corresponding to an electrochemical stability window of 3.35 V, which is much wider than the ≈1.6 V window of H_3PO_4-0.3. The expanded stability window is beneficial for the gassing problem when high-voltage cathodes and low-voltage anodes are used, which promises enhanced energy density as well as cycling stability. The Tafel plot of the Ti electrode is then measured to assess the corrosiveness of the AiCE (Figure 2c). The corrosion potential

Table 1. Comparison about proton-transport kinetics of the representative proton electrolytes in this work.

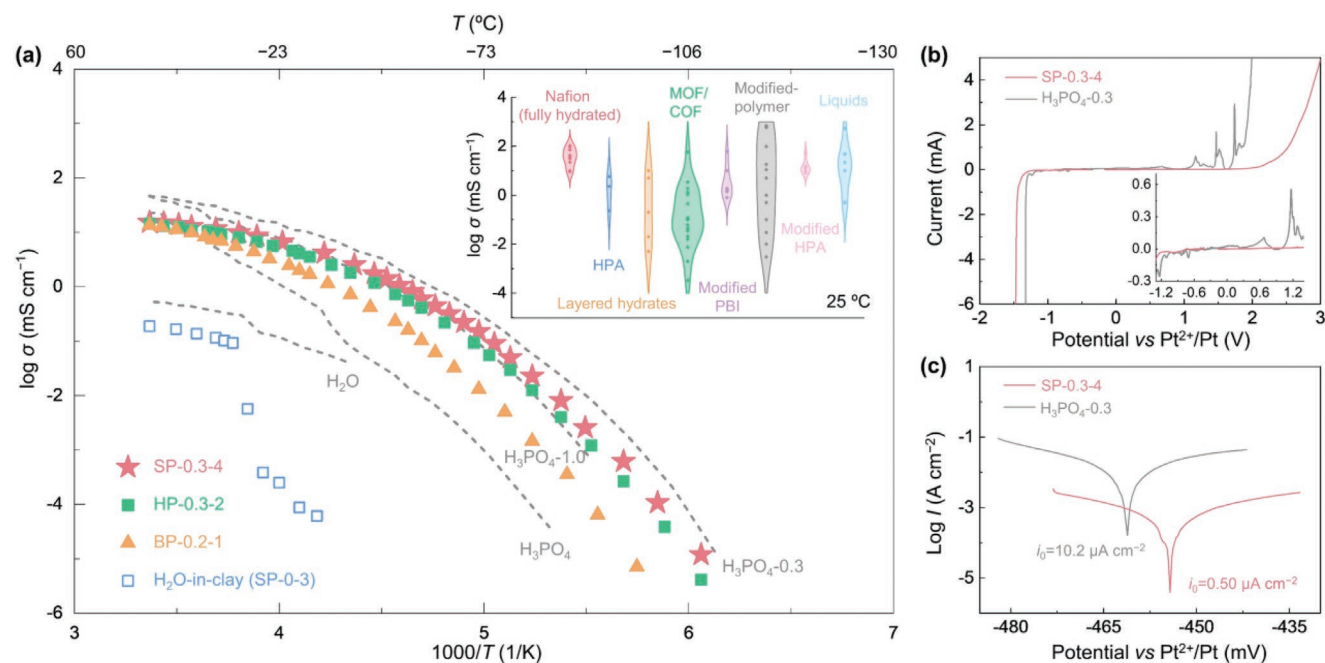| Materials	Proton conductivity at 25 °C [mS cm^{-1}]	Activation energy at 25 °C [eV]	Proton conductivity at −82 °C [mS cm^{-1}]	Activation energy at −82 °C [eV]
SP-0.3-4	15	0.12	0.023	0.65
HP-0.3-2	15	0.15	0.013	0.71
BP-0.2-1	14	0.22	0.001	0.77
H_3PO_4 (100 wt% H_3PO_4)	22	0.46	0.0002	0.88
H_3PO_4-1.0 (85 wt% H_3PO_4)	48	0.28	0.019	0.85
H_3PO_4-0.3 (62 wt% H_3PO_4)	46	0.19	0.070	0.59
H_3PO_4-0 (H_2O)	0.52	0.14	0.005 (−42 °C)	0.28 (−42 °C)

Figure 2. Kinetic and thermodynamic properties of AiCEs. a) The conductivity comparison of AiCEs (SP-0.3-4, HP-0.3-2, and BP-0.2-1) with liquid electrolytes (H_3PO_4, H_3PO_4-0.3, H_3PO_4-1.0, H_2O), and other solid proton electrolytes (violin plots inset). PBI: polybenzimidazole; HPA: heteropoly acid; MOF: metal–organic framework; COF: covalent organic framework. The references are listed in Table S1, Supporting Information. b,c) Comparison of linear scanning voltammetry at 0.1 mV s^{-1} (b) and Tafel curves (c) about the corrosion on metallic titanium foil of SP-0.3-4 and H_3PO_4-0.3.

is suppressed from −462 mV for H_3PO_4-0.3 to −454 mV for SP-0.3-4 (vs Pt^{2+}/Pt). Meanwhile, the corrosion exchange current density is reduced by more than one order of magnitude, from $i_0 = 10.2$ μA cm^{-2} to $i_0 = 0.50$ μA cm^{-2} for SP-0.3-4. These results demonstrate the reduced corrosiveness of SP-0.3-4 toward the Ti current collector.

2.2. Structural Study of AiCE

Structural analyses were conducted to study the interactions between the acid and clay. Scanning electron microscopy (SEM) images show that the pristine sepiolite comprises fibers of ≈100 nm in diameter and several micrometers in length (**Figure 3**a). The X-ray diffraction (XRD) pattern shows broad peaks at 10°–30°, suggesting that the sepiolite loses its crystallinity after reacting with the acid solution (Figure S7a,b, Supporting Information). The newly formed Si—O—P bond[18] in Fourier-transform infrared (FTIR) spectroscopy confirms a chemical reaction between the acid and clay (Figure S7c, Supporting Information). The gel-like material formed exhibits a Young's modulus of 56 MPa and a hardness of 2.4 MPa, similar to elastic polyurethanes,[19] indicating AiCE is a soft solid material (Figure 3b). In situ cryogenic XRD results show no detectable changes in the amorphous structure when the temperature is scanned from room temperature to −83 °C (Figure 3c), implying the proton conductive network can be well maintained in a wide temperature range without a temperature-induced first-order phase transformation, unlike that of bulk water (water ↔ ice) with its associated dramatic reduction of proton conductivity upon freezing. From the analysis in the

above section, the strong acid–acid interactions of the packed-acid mechanism will weaken H-bonds, thereby improving the proton conductivity. Simultaneously, the weaker H-bonds will lead to a stronger O—H bond and better stability.[20] The pair distribution function is then plotted to investigate the bonding length of local structures (Figure 3d). After integrating acid in the clay, the Si—O and Mg—O peaks in the pair distribution function analysis of SP-0.3-4 are weak due to the low fraction of $Mg_2Si_3O_7(OH)_2$ (15 wt%) in SP-4.5-0.3. The newly formed P—O peak in SP-0.3-4 suggests the reaction between phosphoric acid and sepiolite, which is consistent with the results of FTIR. The length of the O—H bond in SP-0.3-4 is shorter than the O—H bond in H_3PO_4-0.3,[21] which rationalizes the enhanced electrochemical and chemical stabilities of SP-0.3-4. Meanwhile, the increased H-bond (OH—O) length in SP-0.3-4 demonstrates the packed acid mechanism and enhanced proton conductivity.

2.3. Proton Batteries with AiCE

The poor cycle life of proton batteries with liquid electrolytes is attributed to several reasons: gassing, dissolution of the current collectors/electrodes by the electrolyte, as well as the subsequent chemical cross-over and contamination of electrodes. Replacing the liquid electrolyte with a noncorrosive and stable solid electrolyte can, in theory, address these problems. However, many all-solid-state batteries suffer from poor interfacial contact, poor ionic conductive network in the electrodes, and difficulty in manufacturing thin-film due to brittleness and sensitivity to moisture. Here, all-solid proton batteries with AiCE as the solid electrolyte (denoted as SPB) are
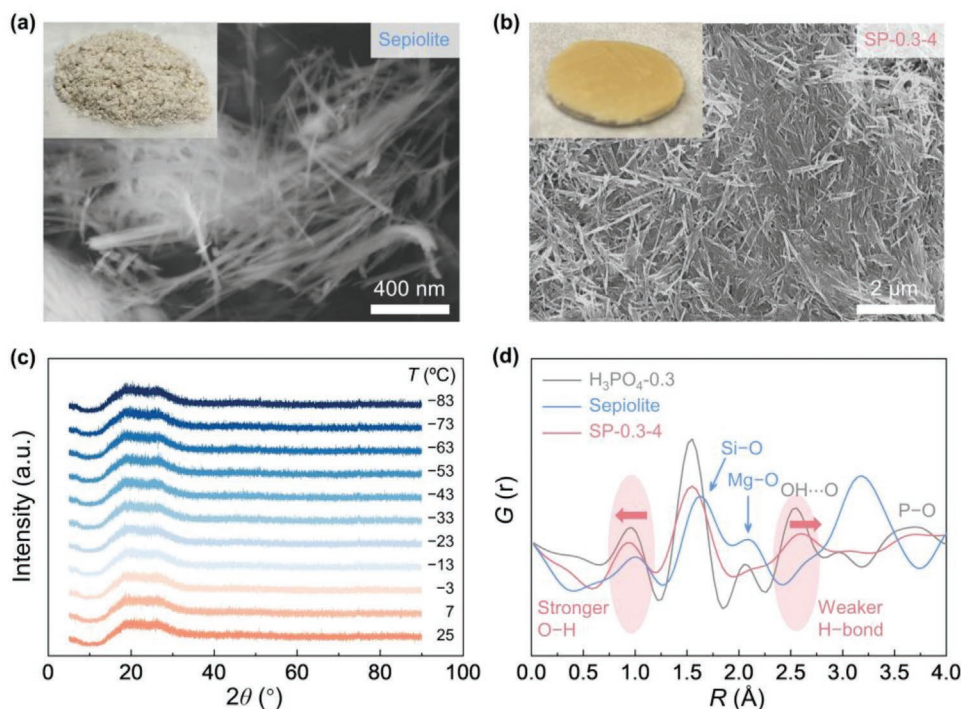
Figure 3. Structural study of AiCE. a) SEM image of the sepiolite. Inset: photograph by a camera. b) SEM image for SP-0.3-4. Inset: photograph by a camera. c) In situ cryogenic XRD patterns for SP-0.3-4. d) Pair distribution function analysis for H_3PO_4-0.3, sepiolite, and SP-0.3-4.

fabricated under air atmosphere, using Ti foil, preprotonated $Cu[Fe(CN)_6]_{0.63} \cdot \square_{0.37} \cdot 3.4H_2O$ (H-TBA) and MoO_3 as the current collector, cathode, and anode, respectively.[4a,c] A proton battery with H_3PO_4-0.3 as the liquid electrolyte was made to be the control (denoted as LPB). Compared with the excellent fluidity of liquid acid, the solid SP-0.3-4 is challenging to be infiltrated into electrode pores to construct a fast proton conductive network. Therefore, a new recipe of AiCE was developed to enhance its fluidity by increasing the liquid amount by 10% during electrolyte synthesis (Table S2, Supporting Information), leading to an increased R ratio from 0.28 (SP-0.3-4) to 0.31 and an increased N ratio from 4 to 5. For this reason, the new solid electrolyte can be termed SP-0.3-5. SP-0.3-5 shows a similar amorphous structure (Figure S8a, Supporting Information) as SP-0.3-4. The Young's modulus (3.6 MPa) and hardness (0.34 MPa) have been successfully decreased by one order of magnitude compared with SP-0.3-4. As a result, the non-Newtonian fluid property of SP-0.3-5 (inset in Figure S8a, Supporting Information) can facilitate its infiltration into the pores of the cathode and anode (Figure S9, Supporting Information). Consequently, the charge transfer resistance of the SPB (4.5 Ω) is comparable to that of the LPB (5 Ω)[4c] (Figure S10a, Supporting Information). It should be noted that the proton conductivity, electrochemical stability window as well as chemical reactivity of SP-0.3-5 are similar to those of SP-0.3-4 (Figure S8b–d, Supporting Information). Although it is crucial for this "non-Newtonian fluid wetting agent" to improve contact without sacrificing electrochemical/chemical stabilities and proton conductivity, it is hard to use SP-0.3-5 as the main solid electrolyte owing to its poor film-forming property (tend to cause a short circuit when applying pressure during battery cell assembly). Therefore,

SP-0.3-5 was used as the "wetting agent" and SP-0.3-4 was used as the "separator membrane" in the following SPBs. The thickness of the SP-0.3-4 membrane is controlled to be ≈150 μm during the electrolyte coating process and is then compressed to ≈20 μm (Figure S9e, Supporting Information) during the cell assembling process (because the soft gel-like electrolyte can be easily squeezed under external pressure, without forming pinholes or cracks).

The SPB shows two voltage plateaus at 1.2 and 0.7 V (**Figure 4**a and Figure S10b, Supporting Information), corresponding to the two redox peaks of MoO_3 (Figure S11, Supporting Information). It provides a specific capacity of 32 mAh g^{-1} at 50 mA g^{-1} (1.5 C), comparable to lead-acid batteries,[22] and maintains 33% capacity even at an extremely high current density of 16 000 mA g^{-1} (720 C, Figure S10c,d, Supporting Information). Such excellent rate performance is comparable to supercapacitors[22] (Figure 4e and Table S5, Supporting Information). Low-temperature tests at −60 °C show the SPB can keep 42% of the room temperature capacity (Figure S12a, Supporting Information) and 77% capacity at 500 mA g^{-1} compared to 50 mA g^{-1} at −35 °C (Figure S12b, Supporting Information). Furthermore, pouch cells of the LPB and the SPB were assembled to examine the gassing problem at room temperature. Severe gassing was seen in the LPB at the open-circuit voltage (discharged state, Figure 4b inset); the current collectors were almost dissolved and purplish liquid leakage was found outside the pouch cell. These problems prevented further cycling tests of the LPB. In contrast, the SPB pouch cell shows no detectable gassing and stable cycling of 1000 cycles at 200 mA g^{-1} (inset in Figure 4b and Figure S13, Supporting Information). It retains 74% of capacity at the 20 000th cycles when cycled at 1000 mA g^{-1} under

**ADVANCED
SCIENCE NEWS**

www.advancedsciencenews.com
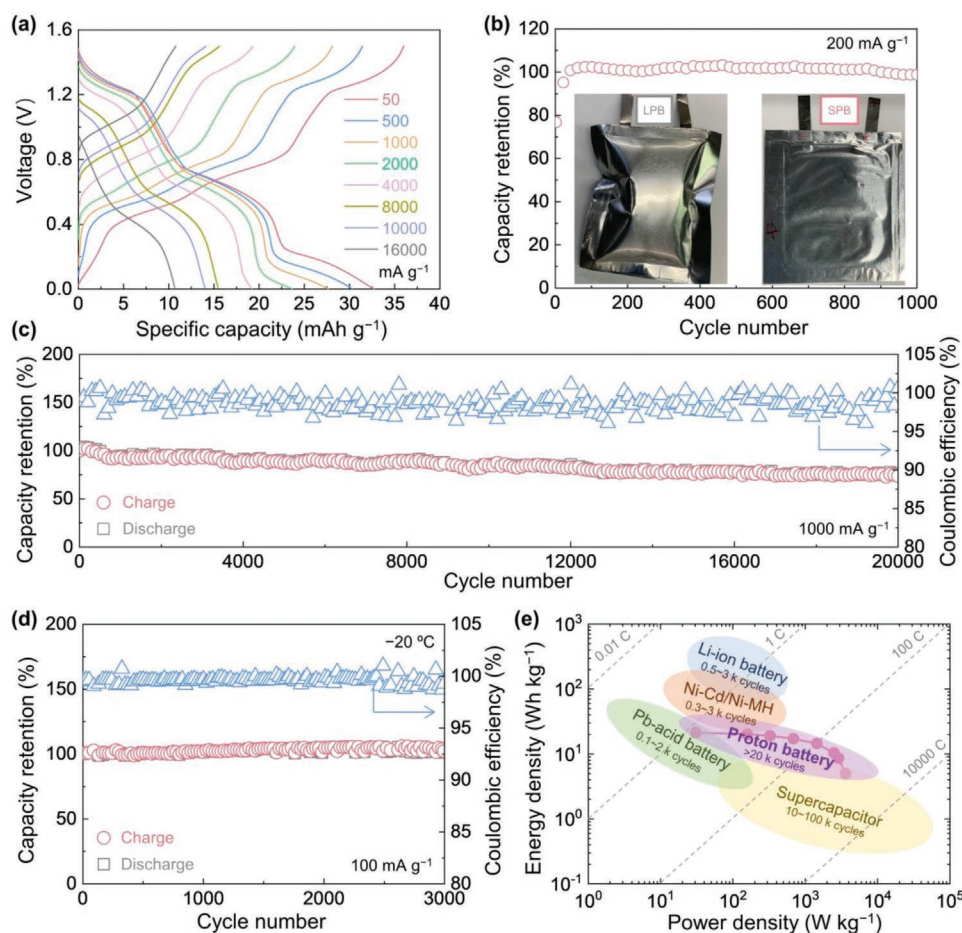
**ADVANCED
MATERIALS**

www.advmat.de

Figure 4. Electrochemical study for proton batteries with AiCE. a) Galvanostatic charge/discharge potential profiles for the SPB at different current rates. b) Cycling performance of the SPB at 200 mA g^{-1}. Insets are the digital images of pouch cells: the LPB after resting for 30 days under 25 °C, and the SPB after 1000 cycles under 25 °C. c,d) Cyclability and Coulombic efficiency of the SPB at 1000 mA g^{-1} under 25 °C (c) and the SPB at 100 mA g^{-1} under −20 °C (d). e) Ragone plot with cyclability for the proton battery, Ni–Cd/Ni–MH battery, Pb–acid battery, supercapacitor, and Li-ion battery (in consideration of energy and power densities for electrodes, the references' values are calculated as double of the real values in cell system, all the specific capacities, and energy densities in this work were calculated by using the total mass of cathode and anode, including active materials, conductive carbon, and binder).

room temperature (Figure 4c), 100% of capacity at the 3000th cycle when cycled at 100 mA g^{-1} under −20 °C (Figure 4d), and 93% of capacity at the 500th cycle when cycled at 50 mA g^{-1} under −35 °C (Figure S12d, Supporting Information). These results demonstrate that replacing the liquid electrolyte with an AiCE can significantly boost the cycle life of the reported proton batteries (Table S6, Supporting Information). The energy and power densities of the SPB and other energy storage technologies are compared in Figure 4e and Table S7, Supporting Information. Proton batteries could fill the gap between Pb–acid batteries and supercapacitors or even replace them. Notably, proton batteries are suitable for several applications: A) The niche market that requires the fast-charging times of supercapacitors but higher energy densities than what supercapacitors can provide. For example, a charge rate of 100 C, a life of >20 000 cycles, and an energy density greater than twofold that of supercapacitors. B) The niche market that requires the energy density of Pb–acid batteries but much longer life and faster charging than what Pb–acid batteries can provide. For

example, tenfold cyclability and >100-fold fast-charging capability of the current Pb–acid batteries. C) The niche market requiring energy storage systems that can work at subzero temperatures. Owing to the excellent cryogenic proton conductivity of AiCE, the proton batteries can operate at the coldest places on earth (e.g., Antarctica) or even for extraterrestrial applications (e.g., Mars or Moon missions). More fundamental studies are performed and discussed next to reveal the mechanisms behind the improved cycling performance.

In situ optical microscopy of the batteries shows that gas bubbles evolve vigorously at both electrode|electrolyte interfaces and current collector|electrolyte interfaces in the LPB (**Figure 5**a,b and Figure S14, Videos S1, S2, Supporting Information). Particularly, a severe gassing problem happened on the anode side, resulting in the separation of electrode material and current collector. In contrast, no gassing can be seen visually for the SPB even after 480 min of cycling (Figure 5c and Video S3, Supporting Information). The corrosion and dissolution of current collectors and electrodes are quantified by inductively
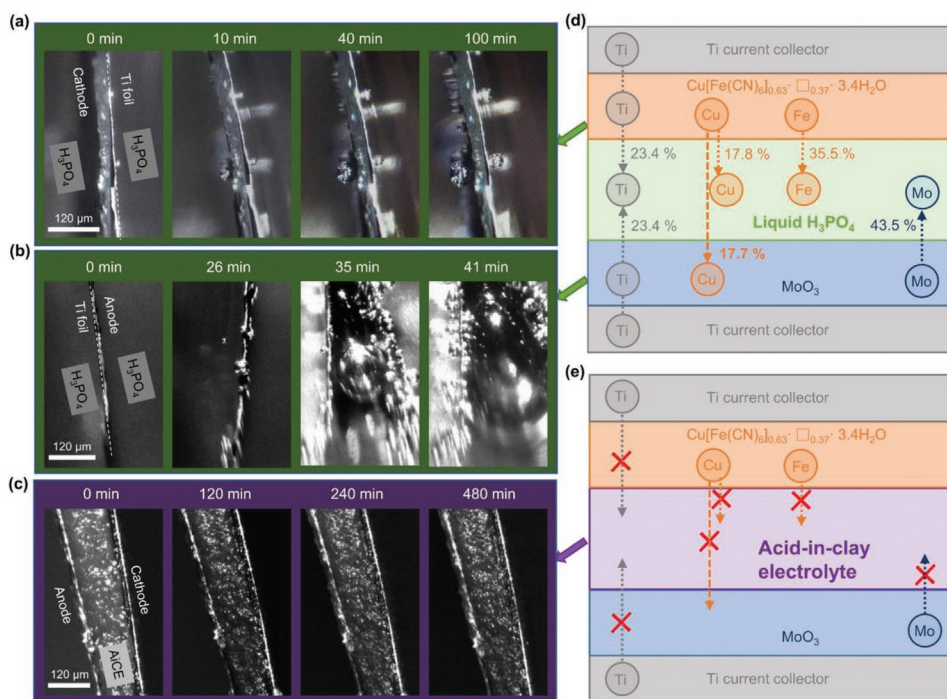
Figure 5. Mechanism study for proton batteries with AiCE. a–c) In situ optical microscopy observation of the LPB (a,b) and the SPB (c) charged and discharged at 4 C. d,e) Schematic diagram of the advantages of the SPB (e) compared with the LPB (d).

coupled plasma mass spectrometry (ICP-MS) of the cycled liquid electrolyte from the LPB. Mo, Cu, Fe, and Ti elements are present in the cycled liquid electrolyte (Table S8, Supporting Information), and their amounts correspond to 43.5% dissolution of MoO_3, 35.5% dissolution of H-TBA, and 46.8% dissolution of Ti current collectors (Figure 5d). It should be mentioned that the calculated Cu element in the liquid electrolyte is 17.8%, which is 17.7% less than the dissolved amount (molar ratio of Cu:Fe is 1:1 in H-TBA). This 17.7% of Cu appears on the anode side due to its cross-over, evidenced by the X-ray photoelectron spectroscopy (XPS). Cu signals appear on the MoO_3 in the LPB after cycling, demonstrating that the Cu elements at the cathode side can pass through the passivation layer, dissolve into the liquid electrolyte, cross over and deposit on the anode side (Figure S15b, Supporting Information). Besides, Ti signals appear on both cathode and anode of the cycled LPB (Figure S15a,b, Supporting Information), implying corrosion and dissolution of current collectors by the liquid acid electrolyte. In contrast, no elements from the cathode can be observed on the cycled MoO_3 in the SPB, and the absence of Mo, Cu, Fe, and Ti elements in the cycled SP-0.3-4 further confirms the prevention of cross-over (Figure 5e and Figure S15c, Supporting Information). Self-discharging analysis at the fully charged state is also a technique to reveal the dissolution and cross-over problems. For the LPB, 12 h rest will cause 55% capacity loss, whereas 83% capacity of the SPB can be maintained after 48 h rest (Figure S16a, Supporting Information), a 13-fold improvement. Besides, the XRD and FTIR analysis of SP-0.3-4 before and after cycling also demonstrates that the average structure and chemical bonding are stable under the long-term operating environment (Figure S16b,c, Supporting Information). Based

on these results, AiCE can prevent gassing, corrosion, and element cross-over, thereby enhancing the cyclability of the proton battery.

2.4. The Universality of the AiCE Approach

To demonstrate university of the AiCE approach, more types of acids (sulfuric acid) and clays (bentonite and halloysite) were investigated. Bentonite and halloysite were chosen for two reasons: first, their structures and chemistries are different but representative of a wide range of clays;[23] second, they have different internal surface areas, thereby different absorption ability (Figure S2a, Supporting Information), allowing the synthesis of AiC compounds with various amounts of clay/acid. Besides phosphoric acid, sulfuric acid is also a widely studied liquid proton conductor and the main proton donor in modified polymer-based proton membranes[7a,24] (Table S1, Supporting Information). The formulas of clays are calculated to be $H_2Al_2O_6Si \cdot 1.19H_2O$ (bentonite) and $H_4Al_2O_9Si_2 \cdot 0.32H_2O$ (halloysite) based on TGA analysis (Figure S2, Supporting Information). Similar to sepiolite, dry bentonite and halloysite are barely malleable to make pinhole/crack-free solid electrolytes. After absorbing water, both clays demonstrate malleability and proton conductivities (Figure S17c,d, more details about the composition ratios are shown in Table S2, Supporting Information). When H_3PO_4 molecules are absorbed into the structure, a similar gel-like phase with low crystallinity can be obtained (Figure S17a,b, Supporting Information), which shows enhanced proton conductivity: up to 15 mS cm^{-1} under room temperature, with the optimized composition of $R = 0.3$

**ADVANCED
SCIENCE NEWS**

www.advancedsciencenews.com

**ADVANCED
MATERIALS**

www.advmat.de

for halloysite (HP-0.3-2), and $R = 0.2$ for bentonite (BP-0.2-1). The cryogenic proton conductivity and the activation energies of both electrolytes are close to that of HP-0.3-2 (Figure 2a and Table S4, Supporting Information). The proton conductivity gradually decreases with decreasing temperatures, and 0.013 mS cm^{-1} (HP-0.3-2) and 0.001 mS cm^{-1} (BP-0.2-1) can be realized at −82 °C (Table 1 and Table S1, Supporting Information). Finally, a 3 M sulfuric acid solution was chosen to synthesize AiCEs with sepiolite, halloysite, and bentonite. A similar trend of structural change, proton conductivity enhancement, and chemical and electrochemical stability improvements demonstrates the universality of the AiCE approach (Figures S18, S19, and Notes S4, S5, Supporting Information).

3. Discussion and Conclusion

Based on our experiments (Figure 1), we see that: 1) Since there are many more types of natural materials with abundant internal surfaces (like clays and woods[25]) than the materials studied in this work, it is reasonable to conjecture that more solid proton electrolytes with superfast proton conductivity and special properties can be synthesized by integrating proton carriers (water and acids) into the hydrophilic networks. The suppression of first-order freezing transition and the associated drastic drop in proton conductivity down to −82 °C is one of the benefits of this approach. Engineering the chemical properties of these internal surfaces could be a universal approach to modifying their bulk properties and achieving unprecedented performances. 2) The acid-in-clay electrolyte can suppress the chemical reaction kinetics of the protons and structural water, resulting in suppressed gassing problem (HER and OER) and suppressed corrosion of electrodes/current collectors. 3) The fading mechanism by element dissolution and cross-over is a long-term issue in redox flow batteries[26] and Li–S batteries.[27] It is also attracting increasing attention in lithium-ion batteries with manganese spinel[28] and nickel-rich layered cathodes.[29] Here, we demonstrate that unwanted element cross-over could also be an overlooked but essential factor for the capacity fading in proton batteries. A solid electrolyte could be an excellent ionic selective membrane to stop element dissolution and cross-over of unwanted cations. 4) AiCE is highly malleable and can be easily made into a fluid-impervious thin membrane with thickness <20 µm, which has the suitable mechanical properties as a separator. Because its modulus can be easily tuned by the amount of water/acid addition, its non-Newtonian flow behavior in the high water/acid addition limit can be utilized to achieve excellent ionic contact with the active material as well. Besides, AiCE is air/moisture tolerant, enabling the battery to be assembled under ambient conditions without using a glovebox. AiCE can be stored and transported easily without a significant drop in performance. 5) The AiCE approach could also be used in many other applications like electrochemical synapse,[30] electrosynthesis,[31] redox flow batteries,[26] CO$_2$ reduction,[32] and NH$_3$ production,[33] with the advantages of fast proton conductivity, improved electrochemical window, free-of-crossover, and reduced corrosiveness.

To summarize, we develop an "acid-in-clay electrolyte" (AiCE) approach to prepare a series of novel proton electrolytes. Owing

to the advantages of superfast proton transport, excellent selectivity, and enhanced stability, we demonstrate the superiority of the proton electrolytes in solving two main challenges in proton batteries: gassing and poor cycling performance. The solid proton batteries show 20 000 stable cycles at 1000 mA g^{-1} with only 26% capacity decay under room temperature, and 3000 stable cycles at 100 mA g^{-1} with almost 100% capacity retention under −20 °C. More broadly, the AiCE approach opens a new avenue for designing and tailoring electrolyte properties for various electrochemical technologies based on proton conduction.

4. Experimental Section

Materials Synthesis: All the phyllosilicate clays, including sepiolite, hydrophilic bentonite, halloysite, 85 wt% phosphoric acid, and 95 wt% sulfuric acid were purchased from Sigma-Aldrich. For a typical synthesis of integrated acid/H$_2$O in clays, a specific concentration of acid and H$_2$O was first mixed to form a uniform solution. Then the solution was ground with the clay powder in a mortar for several minutes to form a gel. More details about the composition ratios are shown in Tables S2 and S3, Supporting Information. Preprotonated TBA (H-TBA) was synthesized by chemical reduction of Cu[Fe(CN)$_6$]$_{0.63}$·□$_{0.37}$·3.4H$_2$O by N$_2$H$_4$ under Ar protection. MoO$_3$ was prepared by a hydrothermal reaction between (NH$_4$)$_6$Mo$_7$O$_{24}$·4H$_2$O and HNO$_3$ solution (more details are shown in previous work[4c]).

Materials Characterizations: In situ XRD with a temperature control stage (PANalytical Empyrean Diffractometer; Cu K_α radiation with wavelength $\lambda = 1.5418$ Å) was used to characterize the phase and the temperature-dependent structural information. Solid electrolytes were assembled in coin cells with a Kapton window that ensures the penetration of an X-ray beam. The measurements were first conducted at 300 K, and then the temperature was set from 300 to 190 K with a 10 K temperature interval, a ramping rate of 2 K min^{-1}, and a 10 min constant temperature rest before each measurement. Pair distribution function measurements were conducted at 11-ID-C beamline at Advanced Photon Source, Argonne National Laboratory. The samples were sealed in capillary tubes. TGA was carried out using TA Instruments, Discovery with a heating rate of 2 °C min^{-1} in air. The SEM (MERLIN VP Compact) was performed to characterize the morphology. The nanoindentation tests were performed using a TI 950 Triboindenter (Hysitron, Inc.), equipped with a Berkovich diamond tip to examine mechanical properties. The hardness and Young's modulus were evaluated based on the Oliver-Pharr method.[34] Inductively coupled plasma optical emission spectrometry (ICP-OES, Perkin Elmer 2100 DV) was applied to analyze the electrolyte compositions. The Brunauer–Emmett–Teller specific surface area of the samples was conducted on a Micrometrics ASAP 2020 physisorption analyzer using the standard N$_2$ adsorption and desorption isotherm measurements at 77 K. XPS was conducted using PHI Versaprobe II system. FTIR was analyzed on Thermo Scientific portable FTIR analyzers. For the ^{1}H solid-state NMR measurements, the sample was packed into a 5 mm NMR tube under a dry nitrogen atmosphere in a glove bag, sealed with tight-fitting caps, and stored in a desiccator. All measurements were performed using a 300 MHz (^{1}H frequency) Varian Direct Drive spectrometer and a Doty broadband Z-spec gradient probe.

Electrochemical Characterizations: To prepare electrodes, active mass, conductive carbon, and binder were mixed with a specific weight ratio of 80:10:10 to form a homogenous slurry, which was spread on commercial Ti foils (10 µm) and dried at 60 °C in a vacuum for 12 h. The active mass loadings for the MoO$_3$ anode and H-TBA cathode were around 2.0 mg cm^{-2} (≈40 µm) and 4.0 mg cm^{-2} (≈15 µm), respectively. The negative:the positive capacity ratio was controlled to be ≈1.0:1.0. For the cells with solid electrolytes, a small amount of SP-0.3-5 was used to wet the electrodes (8 mg cm^{-2}). Then SP-0.3-4 (≈150 µm) was coated uniformly on the surface of the wetted cathode, and the anode

was put on the solid electrolyte. Coin cells were assembled by Digital Pressure Controlled Electric Crimper (MTI, corporation), and pouch cells were sealed by an MSK-11A-S vacuum sealer. Some SP-0.3-4 was squeezed out of the electrodes by the pressure during cell assembling, resulting in a thickness decrease to ≈20 µm. The weight ratio of solid electrolyte:electrodes was 8.1:1.0. The cells with liquid electrolytes were measured in Swagelok cells composed of three electrodes and a pouch cell configuration (polyether-sulfone membrane with 100 µm was used as the membrane, the weight ratio of liquid electrolyte:electrodes was 8.0:1.0), where the detailed procedures were shown in previous work.[4c] All the C-rates in this work were calculated based on the real charge/discharge time. All the specific capacities in this work were calculated using the total mass of cathode and anode, including active materials, conductive carbon, and binder.

Gamry (Reference 3000) electrochemical workstation was used for cyclic voltammetry and also for electrochemical impedance spectroscopy (EIS) from 0.1 Hz to 1 MHz, with a perturbation of 50 mV applied. To measure the electrochemical stability window, linear scanning voltammetry was also performed by electrochemical workstation in Swagelok three-electrode cells with Ti rod as the working and counter electrodes, and Pt wire as the reference electrode. In situ cryogenic EIS measurements were conducted on a homemade physical property measurement system (PPMS)-Gamry linked platform. Two-electrode devices were first made by using stainless steels as the working and counter electrodes and transferred into the cavity of PPMS (Quantum Design PPMS DynaCool). Then PPMS was used to control the temperatures, and the Gamry electrochemical station was used for EIS measurements. In situ optical microscopy measurements were conducted for a homemade cell with an optical micro zoom inspection system (Scienscope, MZ7A). The cell was connected to the Gamry electrochemical workstation for galvanostatic discharge/charge at 4 C at room temperature. For self-discharge measurements, the batteries were first charged to 1.5 V at 50 mA g^{-1}, rested for a specific time (0, 6, 12, 24, 48 h) before discharging to 0 V at 50 mA g^{-1}. The discharge capacity retention could be calculated from each battery at different rest times compared with the one with a rest time of 0 h. For low-temperature measurements, the multi-temperature performance was measured in a biomedical freezer (SANYO) at −20, −35, −50, and −60 °C, where the cells were submerged under isopropyl alcohol solution in a cryogenic storage Dewar mixture. All the cells were tested on a LAND 2001A Cell test system and cycled between 0 and 1.5 V at different temperatures.

Statistical Analysis: Violin plots in the manuscript were used to better illustrate the variations in the data. The shape of each violin plot was a kernel density estimation to illustrate the distribution shape of the data. Wider sections of the violin plot represented a higher probability that members of the population would take on the given value; the thinner sections of the plot represented a lower probability. For the capacity measurements, three cells were assembled and compared, and the cell with the representative average behavior was chosen to demonstrate the performance.

Supporting Information

Supporting Information is available from the Wiley Online Library or from the author.

Acknowledgements

Conflict of Interest

The authors declare no conflict of interest.

Data Availability Statement

The data that support the findings of this study are available from the corresponding author upon reasonable request.

Keywords

[1] M. Li, C. Wang, Z. Chen, K. Xu, J. Lu, *Chem. Rev.* **2020**, *120*, 6783.
[2] a) L. Ye, X. Li, *Nature* **2021**, *593*, 218; b) Y. Chen, Z. Wang, X. Li, X. Yao, C. Wang, Y. Li, W. Xue, D. Yu, S. Y. Kim, F. Yang, A. Kushima, G. Zhang, H. Huang, N. Wu, Y. W. Mai, J. B. Goodenough, J. Li, *Nature* **2020**, *578*, 251.
[3] a) K. Jiao, J. Xuan, Q. Du, Z. Bao, B. Xie, B. Wang, Y. Zhao, L. Fan, H. Wang, Z. Hou, S. Huo, N. P. Brandon, Y. Yin, M. D. Guiver, *Nature* **2021**, *595*, 361; b) M. Winter, B. Barnett, K. Xu, *Chem. Rev.* **2018**, *118*, 11433.
[4] a) X. J. Wu, J. J. Hong, W. Shin, L. Ma, T. C. Liu, X. X. Bi, Y. F. Yuan, Y. T. Qi, T. W. Surta, W. X. Huang, J. Neuefeind, T. P. Wu, P. A. Greaney, J. Lu, X. L. Ji, *Nat. Energy* **2019**, *4*, 123; b) L. Zhou, L. Liu, Z. Hao, Z. Yan, X.-F. Yu, P. K. Chu, K. Zhang, J. Chen, *Matter* **2021**, *4*, 1252; c) H. Jiang, W. Shin, L. Ma, J. J. Hong, Z. X. Wei, Y. S. Liu, S. Y. Zhang, X. Y. Wu, Y. K. Xu, Q. B. Guo, M. A. Subramanian, W. F. Stickle, T. P. Wu, J. Lu, X. L. Ji, *Adv. Energy Mater.* **2020**, *10*, 2000968.
[5] Y. K. Xu, X. Y. Wu, X. L. Ji, *Small Struct.* **2021**, *2*, 2000113.
[6] Y. Sui, X. Ji, *Chem. Rev.* **2021**, *121*, 6654.
[7] a) C. Zhong, B. Liu, J. Ding, X. R. Liu, Y. W. Zhong, Y. Li, C. B. Sun, X. P. Han, Y. D. Deng, N. Q. Zhao, W. B. Hu, *Nat. Energy* **2020**, *5*, 440; b) X. Wang, R. S. Chandrabose, Z. Jian, Z. Xing, X. Ji, *J. Electrochem. Soc.* **2016**, *163*, A1853.
[8] a) R. Emanuelsson, M. Sterby, M. Stromme, M. Sjodin, *J. Am. Chem. Soc.* **2017**, *139*, 4828; b) Y. Xu, X. Wu, H. Jiang, L. Tang, K. Y. Koga, C. Fang, J. Lu, X. Ji, *Angew. Chem., Int. Ed.* **2020**, *59*, 22007.
[9] O. Borodin, J. Self, K. A. Persson, C. Wang, K. Xu, *Joule* **2020**, *4*, 69.
[10] a) T. Ogawa, H. Ohashi, T. Tamaki, T. Yamaguchi, *Chem. Phys. Lett.* **2019**, *731*, 136627; b) T. Ogawa, T. Aonuma, T. Tamaki, H. Ohashi, H. Ushiyama, K. Yamashita, T. Yamaguchi, *Chem. Sci.* **2014**, *5*, 4878.
[11] P. F. Kerr, *Clays Clay Miner.* **1952**, *1*, 19.
[12] a) J. S. J. Van Deventer, J. L. Provis, P. Duxson, *Miner. Eng.* **2012**, *29*, 89; b) P. Duxson, A. Fernández-Jiménez, J. L. Provis, G. C. Lukey, A. Palomo, J. S. J. van Deventer, *J. Mater. Sci.* **2006**, *42*, 2917; c) R. M. Novais, R. C. Pullar, J. A. Labrincha, *Prog. Mater. Sci.* **2020**, *109*, 100621.
[13] H. H. Murray, *Clay Miner.* **1999**, *34*, 39.

**ADVANCED
SCIENCE NEWS**

www.advancedsciencenews.com

**ADVANCED
MATERIALS**

www.advmat.de

[14] E. Galán, *Clay Miner.* **1996**, *31*, 443.

[15] L. Vilciauskas, M. E. Tuckerman, G. Bester, S. J. Paddison, K. D. Kreuer, *Nat. Chem.* **2012**, *4*, 461.

[16] J. P. Melchior, G. Majer, K. D. Kreuer, *Phys. Chem. Chem. Phys.* **2016**, *19*, 601.

[17] J. A. Hurd, R. Vaidhyanathan, V. Thangadurai, C. I. Ratcliffe, I. L. Moudrakovski, G. K. Shimizu, *Nat. Chem.* **2009**, *1*, 705.

[18] M. R. Ahsan, M. A. Uddin, M. G. Mortuza, *Indian J. Pure Appl. Phys.* **2005**, *43*, 89.

[19] S. Chizhik, Z. Huang, V. Gorbunov, N. Myshkin, V. Tsukruk, *Langmuir* **1998**, *14*, 2606.

[20] S. J. Grabowski, *Chem. Phys. Lett.* **2001**, *338*, 361.

[21] E. Tsuchida, *J. Phys. Soc. Jpn.* **2006**, *75*, 054801.

[22] a) V. Aravindan, J. Gnanaraj, Y. S. Lee, S. Madhavi, *Chem. Rev.* **2014**, *114*, 11619; b) M. M. Kabir, D. E. Demirocak, *Int. J. Energy Res.* **2017**, *41*, 1963.

[23] J.-H. Yang, J.-H. Lee, H.-J. Ryu, A. A. Elzatahry, Z. A. Alothman, J.-H. Choy, *Appl. Clay Sci.* **2016**, *130*, 20.

[24] Z. Guo, J. Huang, X. Dong, Y. Xia, L. Yan, Z. Wang, Y. Wang, *Nat. Commun.* **2020**, *11*, 959.

[25] a) C. Yang, Q. Wu, W. Xie, X. Zhang, A. Brozena, J. Zheng, M. N. Garaga, B. H. Ko, Y. Mao, S. He, Y. Gao, P. Wang, M. Tyagi, F. Jiao, R. Briber, P. Albertus, C. Wang, S. Greenbaum, Y. Y. Hu, A. Isogai, M. Winter, K. Xu, Y. Qi, L. Hu, *Nature* **2021**, *598*, 590; b) T. Li, C. Chen, A. H. Brozena, J. Y. Zhu, L. Xu, C. Driemeier, J. Dai, O. J. Rojas, A. Isogai, L. Wagberg, L. Hu, *Nature* **2021**, *590*, 47.

[26] M. Park, J. Ryu, W. Wang, J. Cho, *Nat. Rev. Mater.* **2016**, *2*, 16080.

[27] W. J. Xue, Z. Shi, L. M. Suo, C. Wang, Z. A. Wang, H. Z. Wang, K. P. So, A. Maurano, D. W. Yu, Y. M. Chen, L. Qie, Z. Zhu, G. Y. Xu, J. Kong, J. Li, *Nat. Energy* **2019**, *4*, 374.

[28] Y. Huang, Y. Dong, S. Li, J. Lee, C. Wang, Z. Zhu, W. Xue, Y. Li, J. Li, *Adv. Energy Mater.* **2020**, *11*, 2000997.

[29] a) M. Yoon, Y. Dong, J. Hwang, J. Sung, H. Cha, K. Ahn, Y. Huang, S. J. Kang, J. Li, J. Cho, *Nat. Energy* **2021**, *6*, 362; b) W. Xue, M. Huang, Y. Li, Y. G. Zhu, R. Gao, X. Xiao, W. Zhang, S. Li, G. Xu, Y. Yu, P. Li, J. Lopez, D. Yu, Y. Dong, W. Fan, Z. Shi, R. Xiong, C.-J. Sun, I. Hwang, W.-K. Lee, Y. Shao-Horn, J. A. Johnson, J. Li, *Nat. Energy* **2021**, *6*, 495.

[30] M. Onen, N. Emond, J. Li, B. Yildiz, J. A. Del Alamo, *Nano Lett.* **2021**, *21*, 6111.

[31] M. A. Shipman, M. D. Symes, *Catal. Today* **2017**, *286*, 57.

[32] O. G. Sánchez, Y. Y. Birdja, M. Bulut, J. Vaes, T. Breugelmans, D. Pant, *Curr. Opin. Green Sustainable Chem.* **2019**, *16*, 47.

[33] G. Qing, R. Ghazfar, S. T. Jackowski, F. Habibzadeh, M. M. Ashtiani, C. P. Chen, M. R. Smith3rd, T. W. Hamann, *Chem. Rev.* **2020**, *120*, 5437.

[34] W. C. Oliver, G. M. Pharr, *J. Mater. Res.* **2004**, *19*, 3.

2202063 (10 of 10)

ADVANCED MATERIALS

Supporting Information

Acid-in-Clay Electrolyte for Wide-Temperature-Range and Long-Cycle Proton Batteries

Shitong Wang, Heng Jiang, Yanhao Dong, David Clarkson, He Zhu, Charles M. Settens, Yang Ren, Thanh Nguyen, Fei Han, Weiwei Fan, So Yeon Kim, Jianan Zhang, Weijiang Xue, Sean K. Sandstrom, Guiyin Xu, Emre Tekoglu, Mingda Li, Sili Deng, Qi Liu, Steven G. Greenbaum, Xiulei Ji,* Tao Gao,* and Ju Li*

ADVANCED MATERIALS

Supporting Information

Acid-in-Clay Electrolyte for Wide-Temperature-Range and Long-Cycle Proton Batteries

Shitong Wang, Heng Jiang, Yanhao Dong, David Clarkson, He Zhu, Charles M. Settens, Yang Ren, Thanh Nguyen, Fei Han, Weiwei Fan, So Yeon Kim, Jianan Zhang, Weijiang Xue, Sean K. Sandstrom, Guiyin Xu, Emre Tekoglu, Mingda Li, Sili Deng, Qi Liu, Steven G. Greenbaum, Xiulei Ji*, Tao Gao*, and Ju Li*

Supplementary Figures S1~S19
Supplementary Tables S1~S8
Supplementary Notes S1~S5
Supplementary References 1~81
Supplementary Videos S1~S3

Supplementary Figures

1:1 type

2:1 type

▲ Tetrahedral SiO₄ (or AlO₄)

■ Octahedral AlO₆ (or MgO₆)

● Structural water:
1) crystallization water (H_2O);
2) structural pseudo-water (−OH group, hydroxide or hydronium)
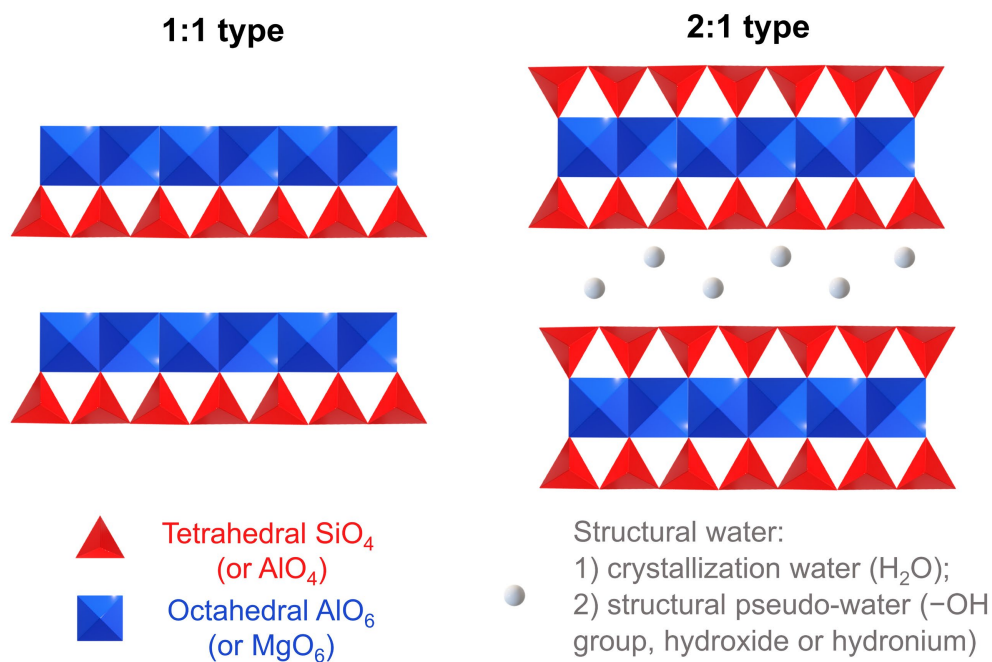
Figure S1 Schematic diagram about the crystal structural of typical clays.

(a)

Sepiolite: 112.9 m² g⁻¹
Halloysite: 37.4 m² g⁻¹
Bentonite: 5.0 m² g⁻¹

(b)

Sepiolite
Halloysite
Bentonite
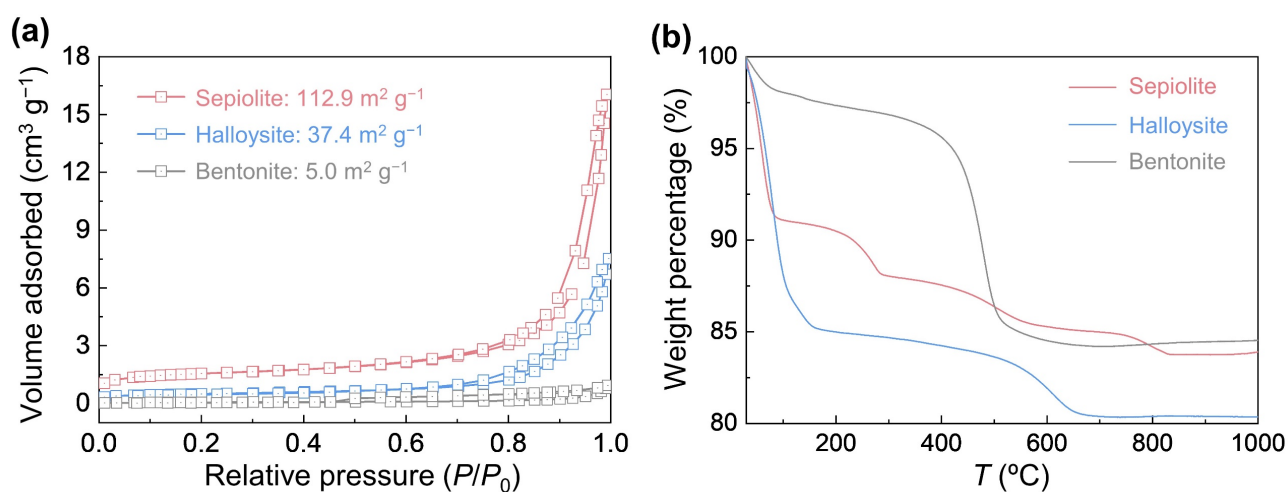
Figure S2 (a) BET surface area analysis and (b) Thermogravimetric analysis of sepiolite, bentonite, and halloysite clays.
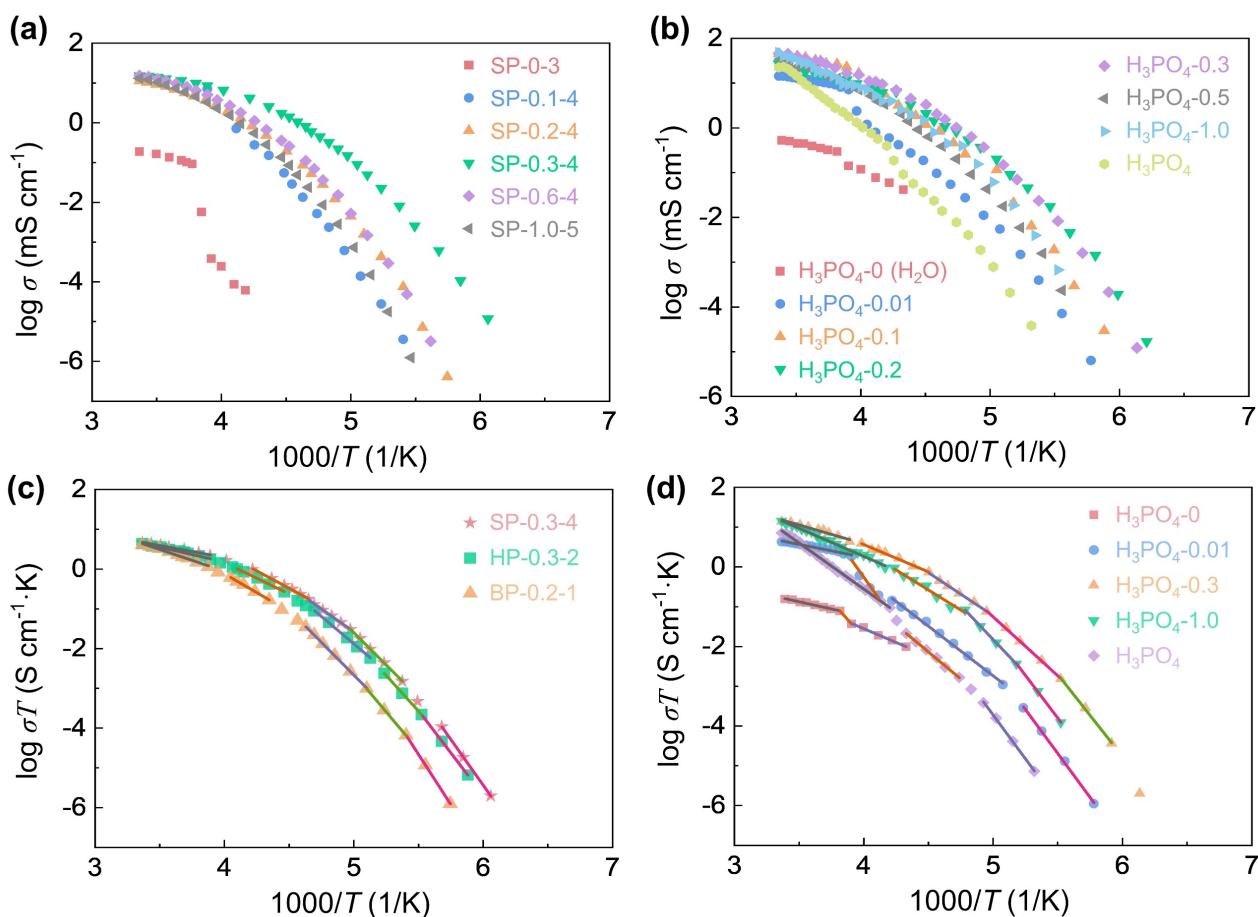
Figure S3 Comparison of proton conductivity for (a) sepiolite-based AiCEs and (b) H_3PO_4 with different concentrations, (c, d) linear fitting for the calculation of activation energy in **Table S4**.

AlO_6 (or MgO_6)

SiO_4 (or AlO_4)

Clay framework

PO_4

Phosphate acid solution

Confined-acid effect

$x[SiO_4]+y[AlO_6]+z[PO_4]−qH_2O \rightarrow$

$[−(Si−O)_x−(Al−O)_y−(P−O)_z−]_n·mH_2O$

$x/y/z$: the Si/Al/P ratio

n: the degree of geopolymerization

Acid-in-clay membrane
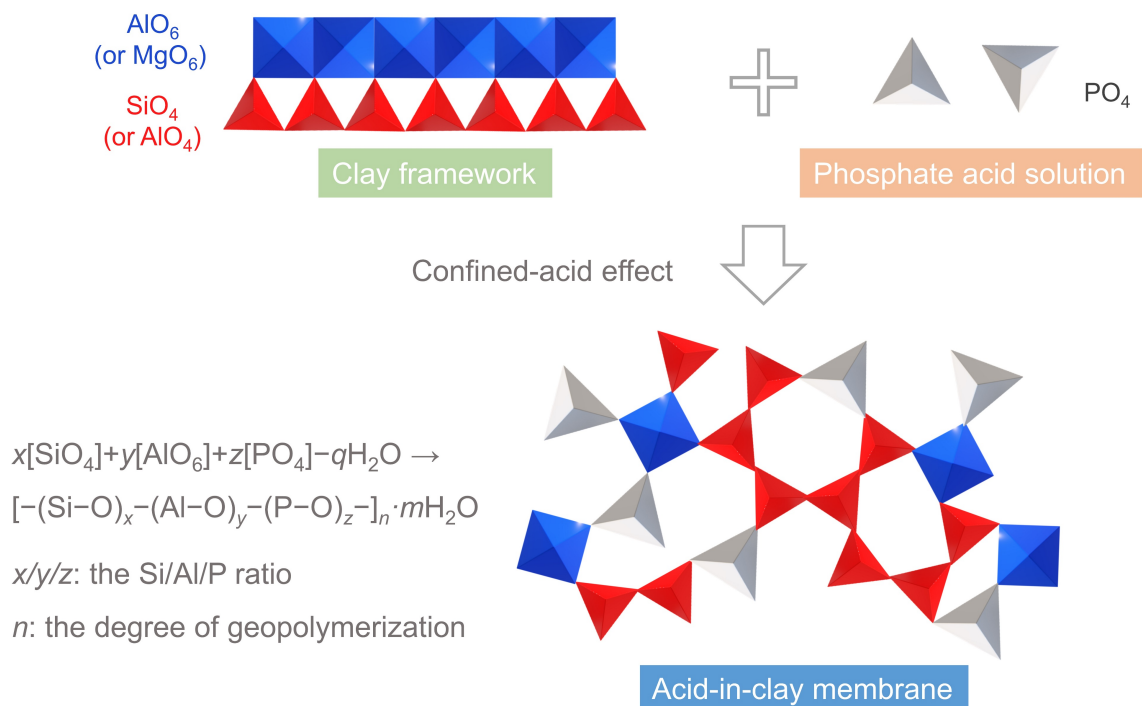
Figure S4 Schematic diagram illustrating the empirical reaction between acid and clay[1].
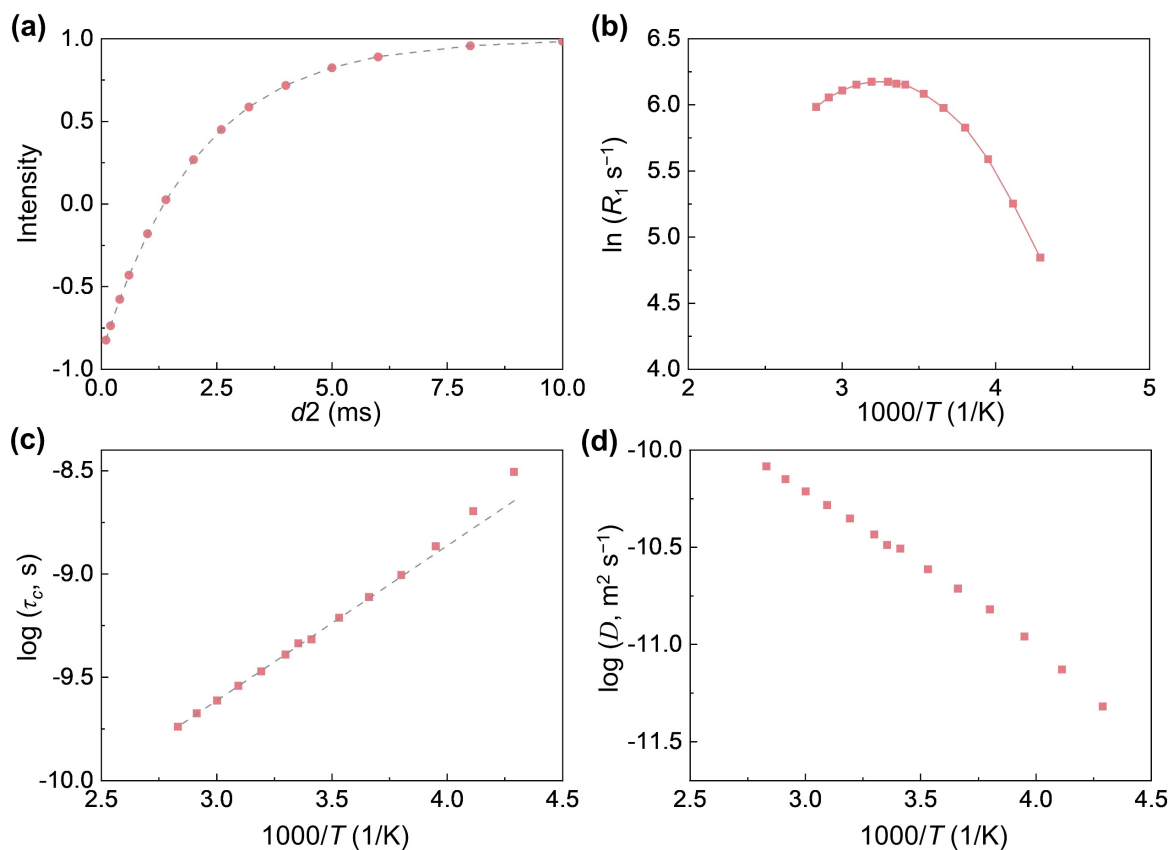
Figure S5 The activation energy and diffusion coefficient analysis via ^{1}H NMR. (a) Relaxation time T_1, (b) spin lattice relaxation rate R_1, (c) proton relaxation correlation times and (d) calculated diffusion coefficients of for SP-0.3-4. More analysis is shown in **Note S1**.
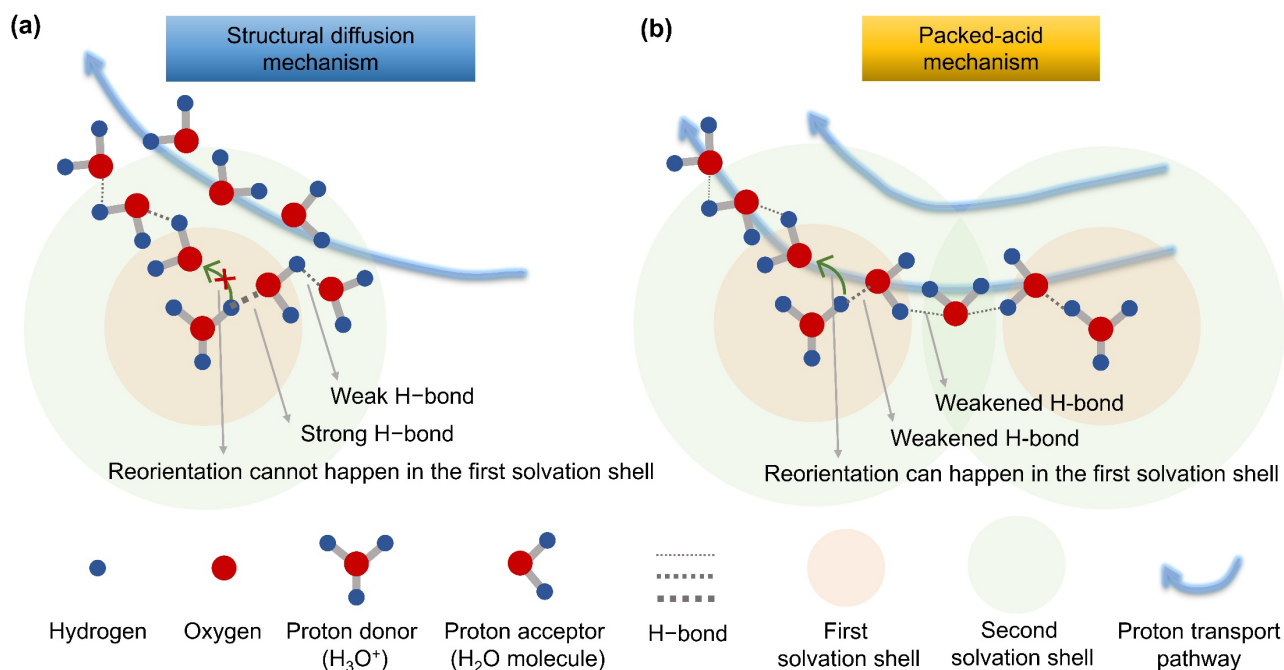
Figure S6 Comparison of the (a) structural diffusion mechanism and (b) packed-acid mechanism. Further analysis is shown in **Note S2**.
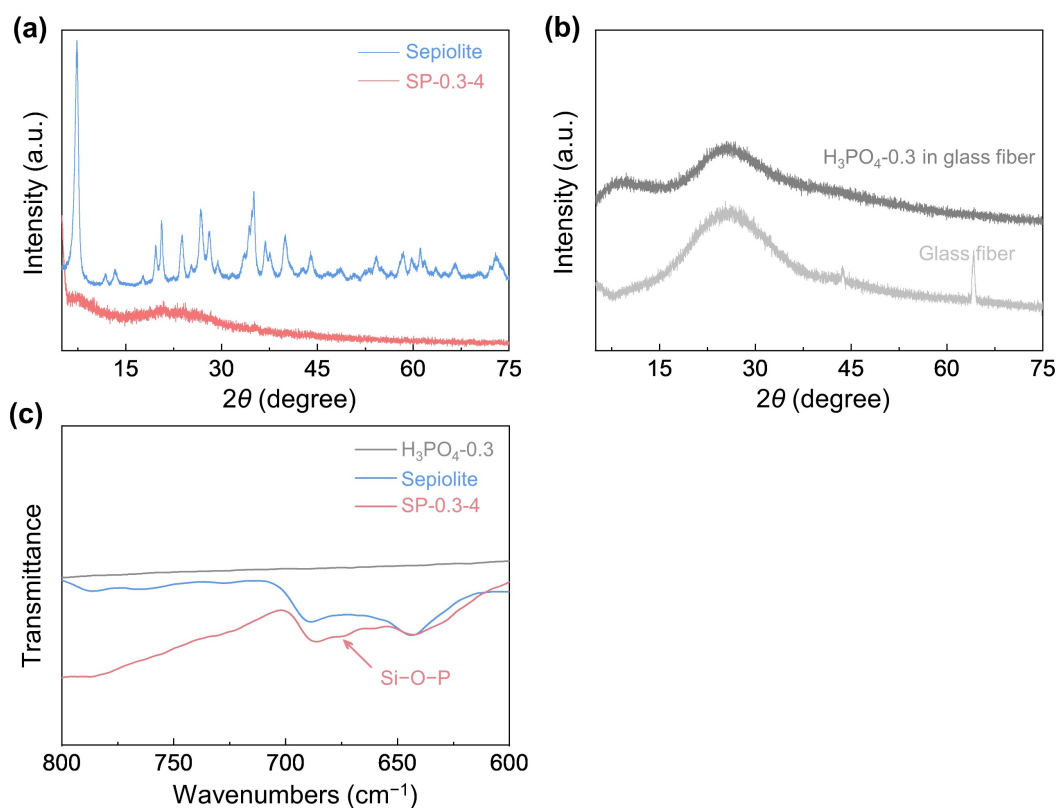
Figure S7 XRD comparison for (a) sepiolite, SP-0.3-4, (b) H₃PO₄-0.3. (c) Fourier-transform infrared spectroscopy (FTIR) comparison for SP-0.3-4, sepiolite and H₃PO₄-0.3.
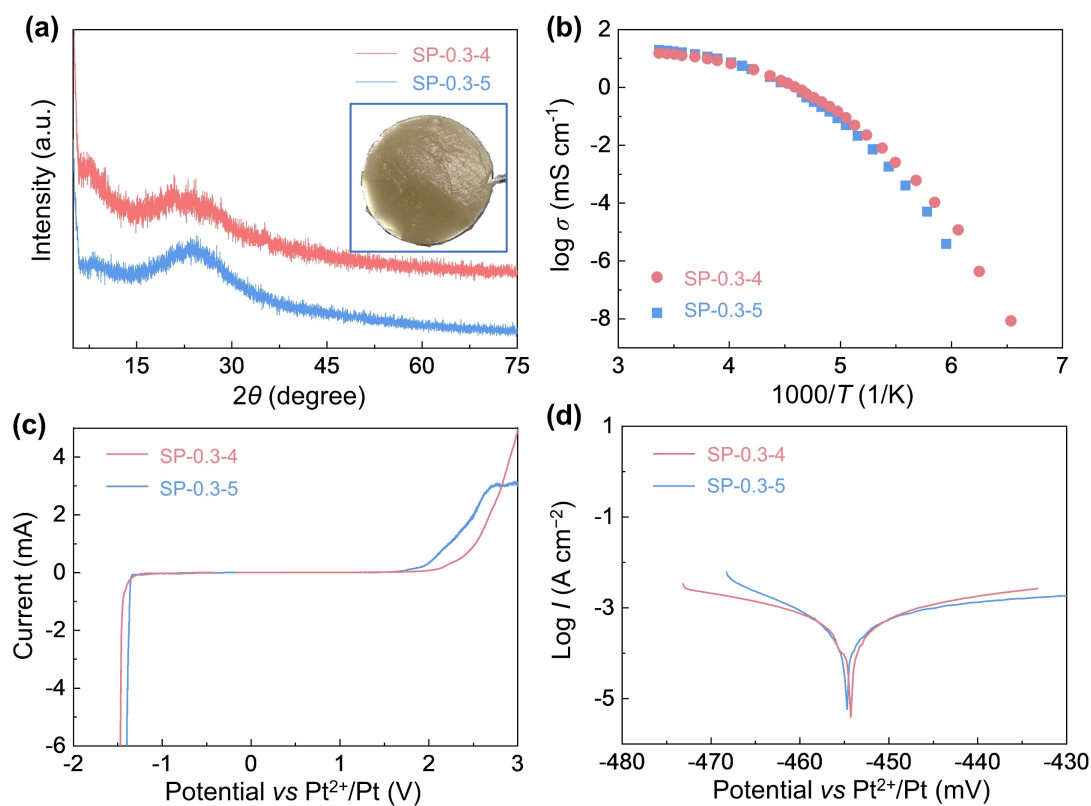
Figure S8 Comparison between SP-0.3-4 and SP-0.3-5. (a) XRD Inset: photograph of SP-0.3-5 by a camera. (b) Proton conductivity, (c) linear scanning voltammetry at $0.1\ mV\ s^{-1}$, and (d) Tafel curves about the corrosion on metallic titanium foil.
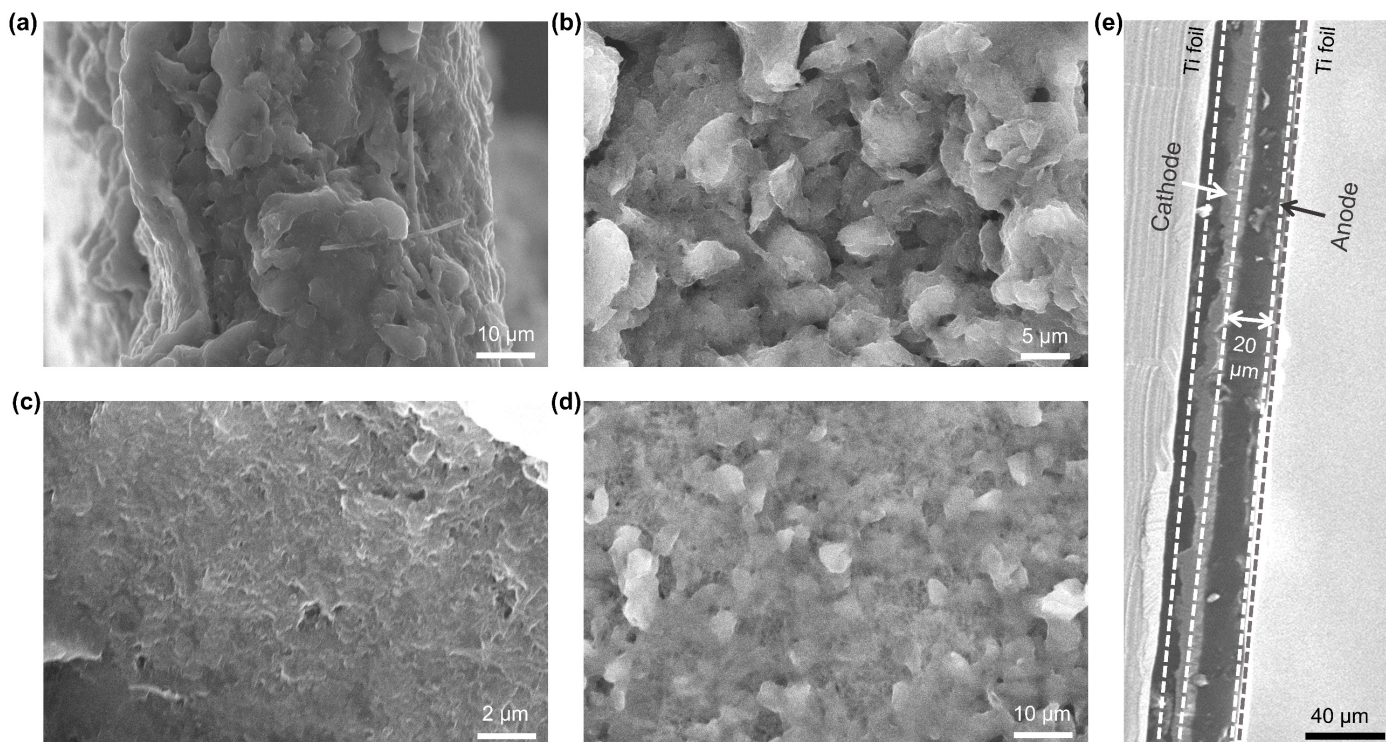
Figure S9 SEM study for the interfacial contact between electrodes and SP-0.3-5. (a) Cross-section and (b) top view of the HTBA cathode, (c) cross-section and (d) top view of the MoO₃ anode, respectively. (e) Cross-section showing the thickness of solid electrolyte in the assembled battery.
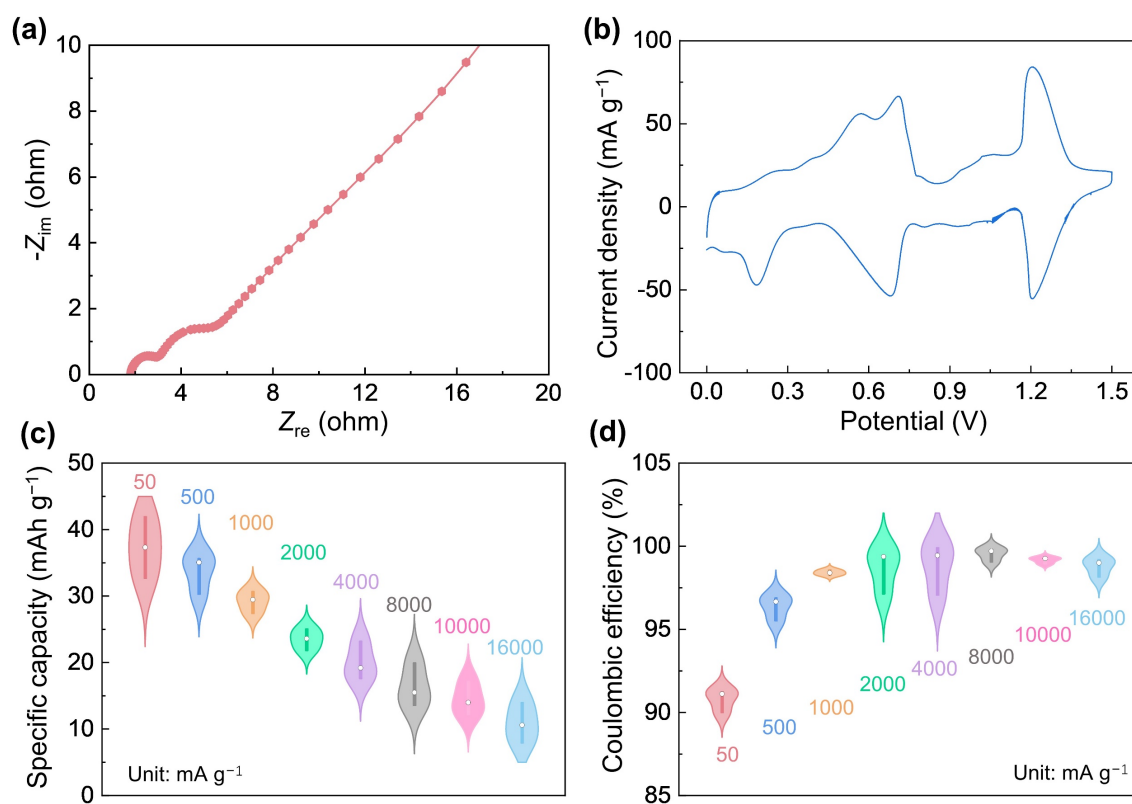
Figure S10 (a) EIS analysis and (b) CV curve at 0.2 mV s⁻¹, (c) Rate capacities and (d) Coulombic efficiencies at 50, 500, 1000, 2000, 4000, 8000, 10000 and 16000 mA g⁻¹, respectively, for SPB under room temperature. Three repeated cells were measured with the median number analysis in (c) and (d).
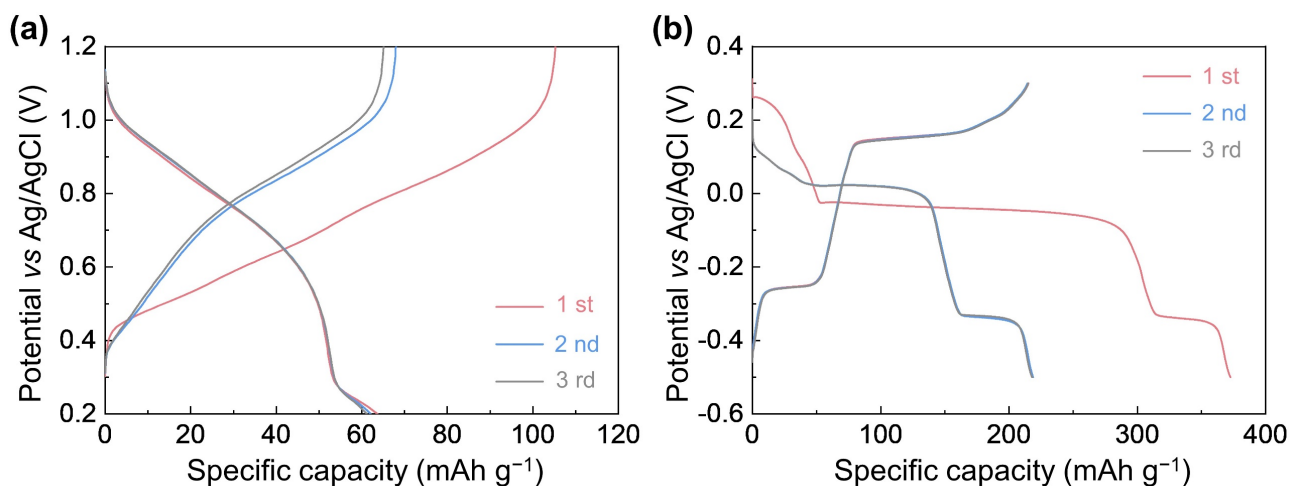
Figure S11 Galvanostatic discharge/charge profiles for (a) H-TBA cathode and (b) MoO_3 anode at 1000 mA g^{-1} in Swagelok® three-electrode cells using H_3PO_4-0.3 as the electrolyte.
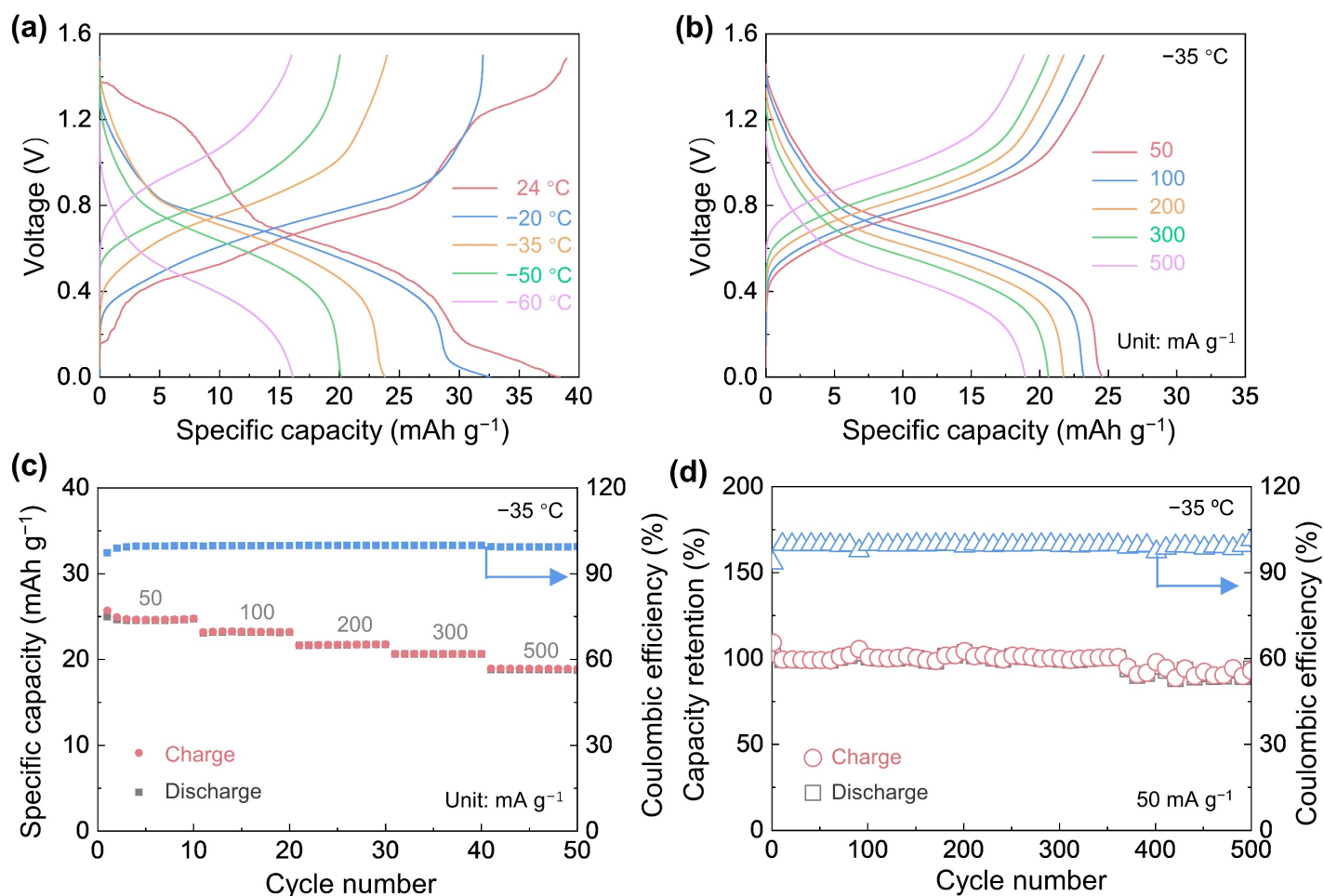
Figure S12 (a) Galvanostatic discharge/charge profiles of SPB at 50 mA g^{-1} under 24 °C, −20 °C, −35 °C, −50 °C and −60 °C, respectively. (b) Galvanostatic discharge/charge profiles and (c) rate performances of SPB under −35 °C at 50, 100, 200, 300 and 500 mA g^{-1}, respectively. (d) Cycling performance of SPB at 50 mA g^{-1} under −35 °C.
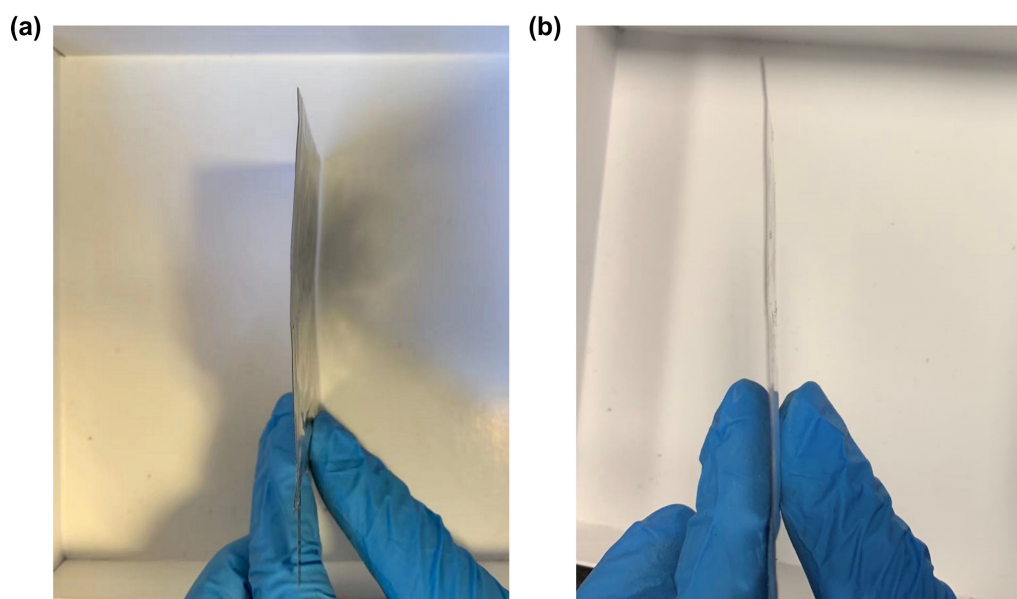
Figure S13 Photos for SPB pouch cell (a) before and (b) after 1000 cycles in **Figure 3b**.
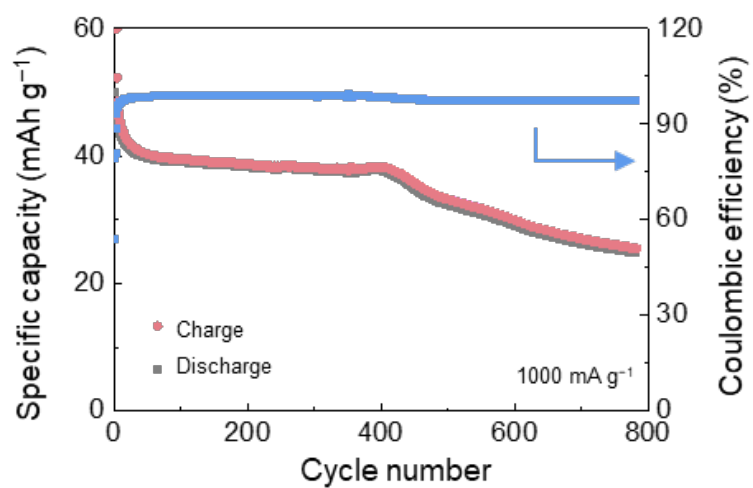
Figure S14 LPB in Swagelok® three-electrodes configuration cycled at 1000 mA g^{-1}, which is further used for mechanism study.
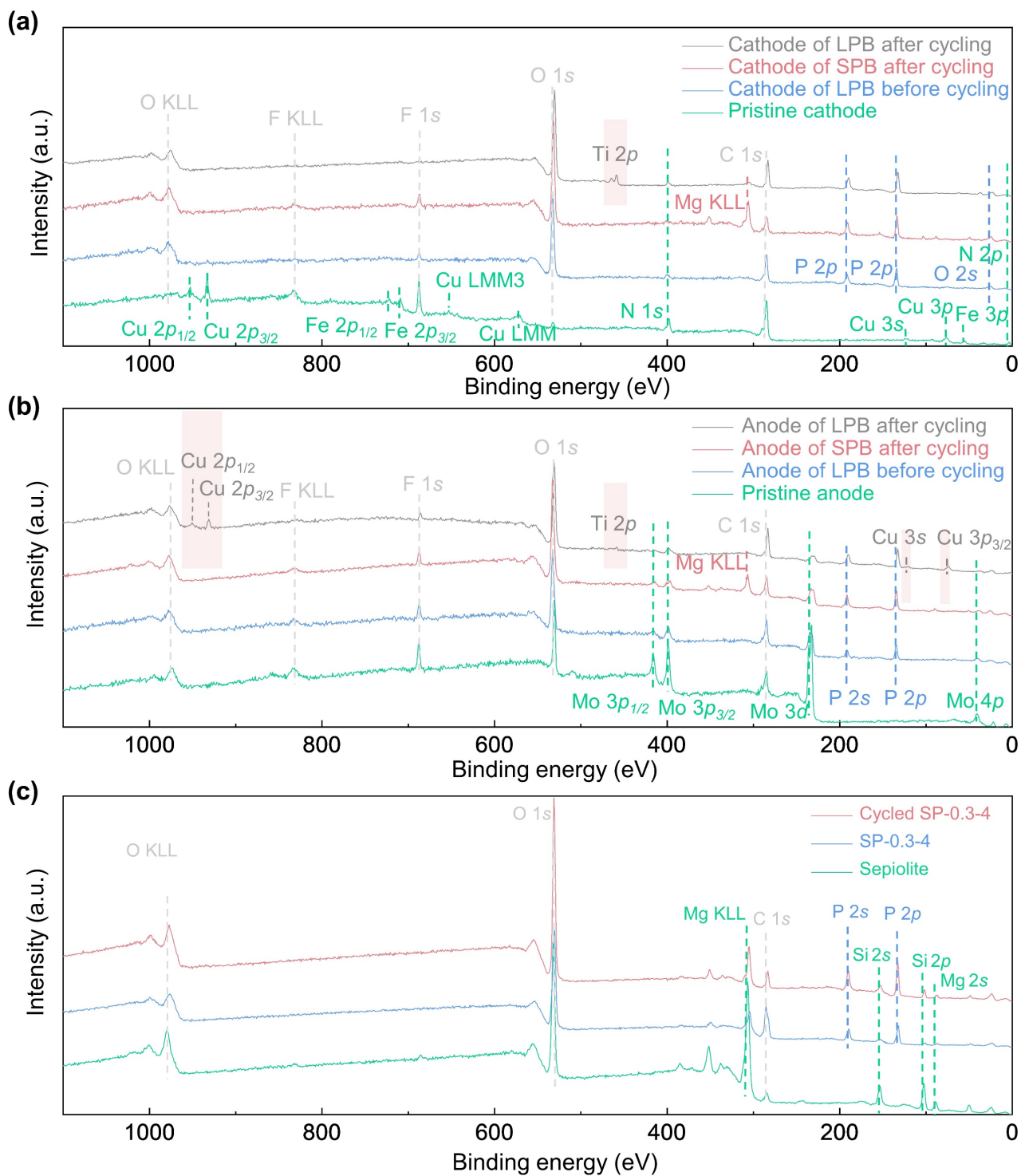
Figure S15 XPS analysis for the pristine, before and after cycling of (a) HTBA cathode and (b) MoO₃ anode. (c) XPS analysis for cycled SP-0.3-4 compared with pristine SP-0.3-4 and sepiolite. More analysis is shown in **Note S3**.
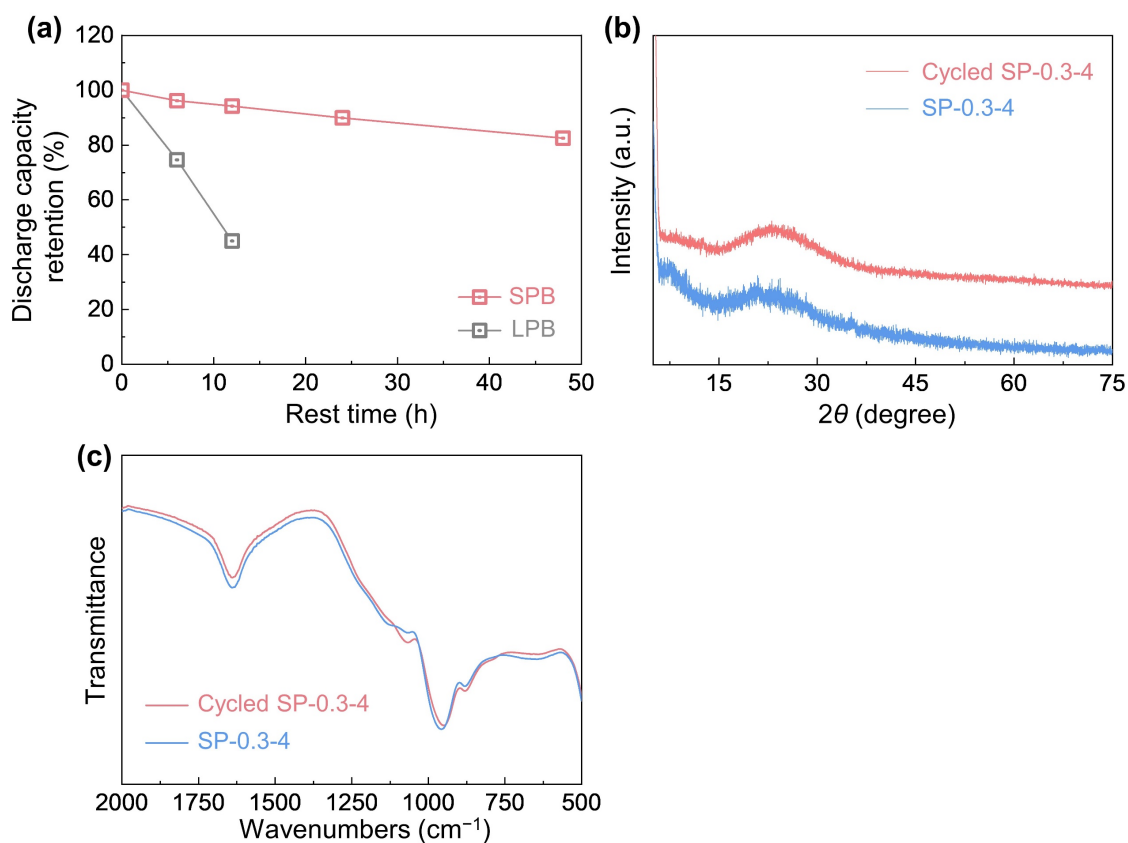
Figure S16 (a) Self-discharge measurements for LPB and SPB, (b) XRD, (c) FTIR analysis for SP-0.3-4 before and after cycling.
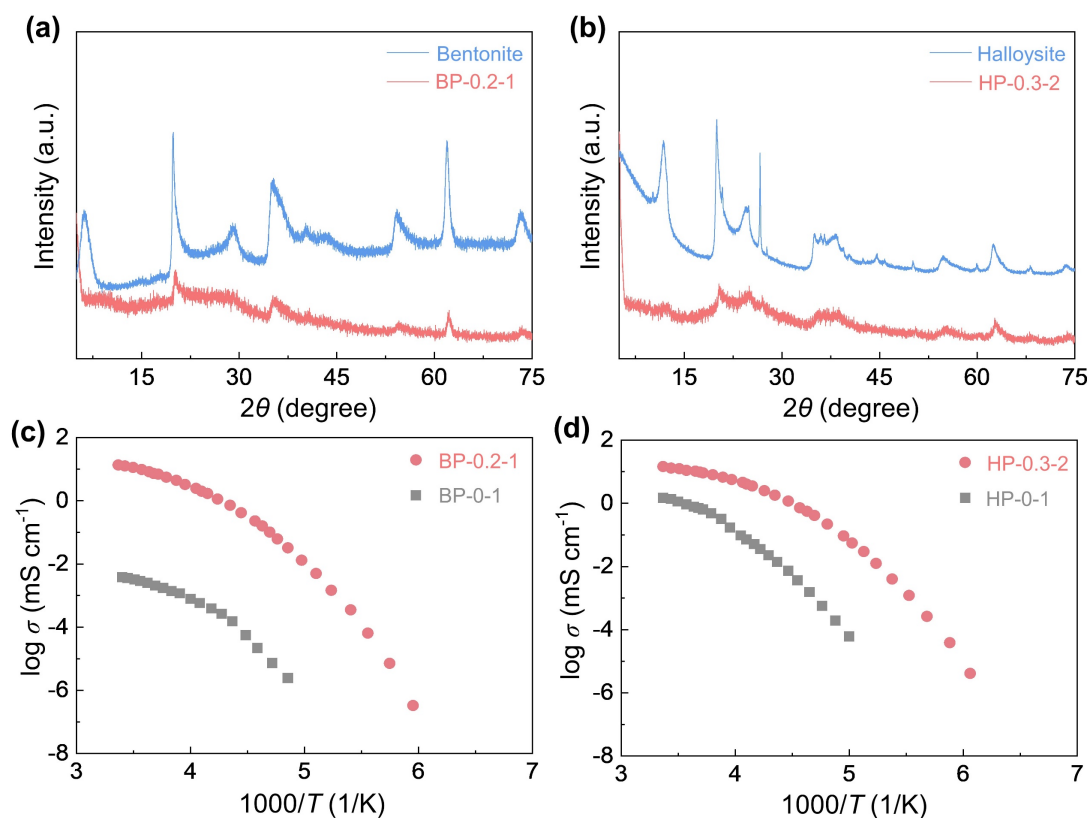
Figure S17 XRD patterns for (a) bentonite and BP-0.2-1, and (b) halloysite and HP-0.3-2. Comparison of proton conductivity for (c) bentonite-based AiCEs and (d) halloysite-based AiCEs.
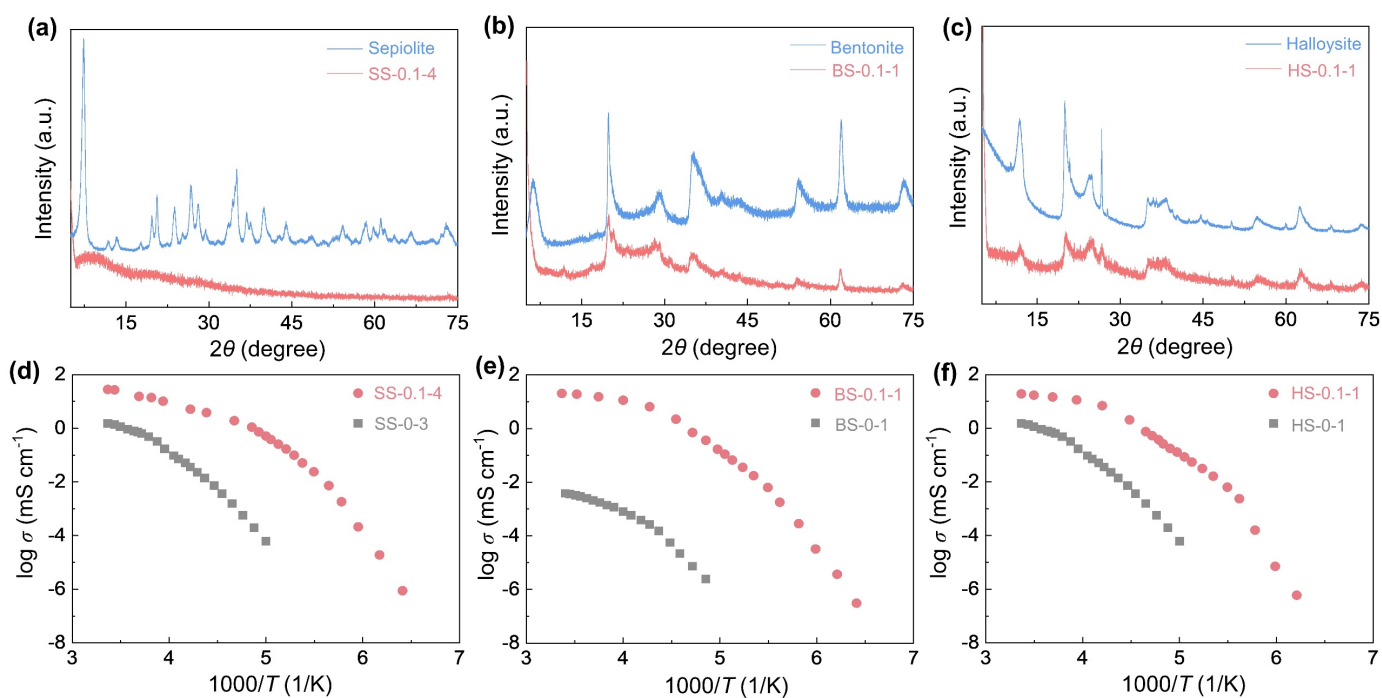
Figure S18 XRD patterns of (a) sepiolite and SS-0.1-4, (b) bentonite and BS-0.1-1, and (c) halloysite and HS-0.1-1. Comparison of proton conductivity for (d) sepiolite-based AiCEs, (e) bentonite-based AiCEs, and (f) halloysite-based AiCEs. Further analysis is provided in **Note S4**.
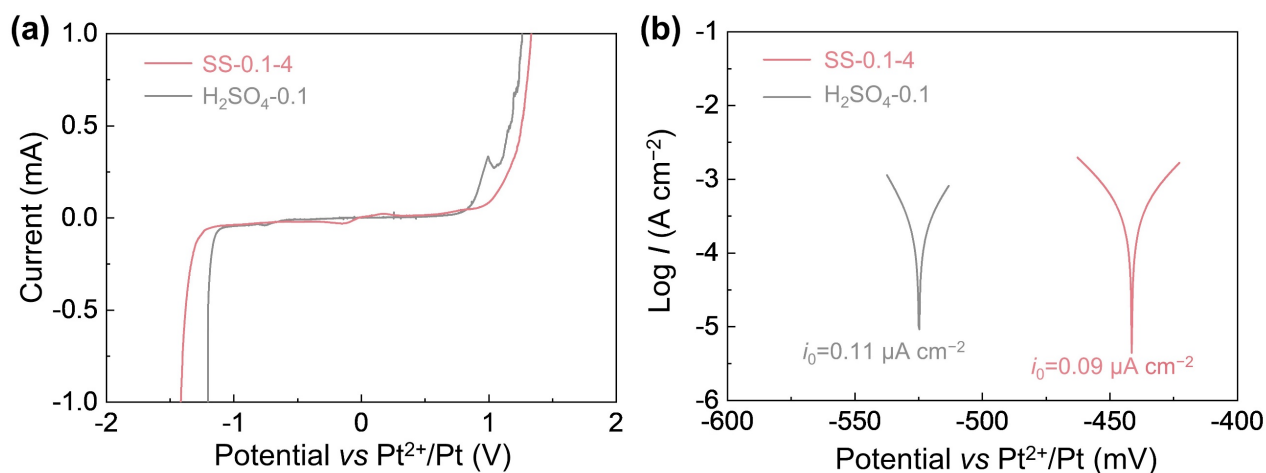
Figure S19 Comparison of (a) linear scanning voltammetry at 0.1 mV s^{-1} and (b) Tafel curves of the corrosion on metallic titanium foil of SS-0.1-4 and H$_2$SO$_4$-0.1. More analysis is given in **Note S5**.

Supplementary Tables

Table S1 Comparison of proton conductivities for room-temperature and low-temperature proton conductors.

Types	Materials	Proton conductivity at room temperature (mS cm^{-1})	Proton conductivity at low temperature (mS cm^{-1})	References
AiCE	SP-0.3-4	**15**	**0.023 (−82 °C)**	
	HP-0.3-2	**15**	**0.013 (−82 °C)**	**This work**
	BP-0.2-1	**14**	**0.001 (−82 °C)**	
Liquid	H$_3$PO$_4$-0.3 (62 wt% H$_3$PO$_4$)	46	0.07 (−82 °C)	
	H$_3$PO$_4$-1.0 (85 wt% H$_3$PO$_4$)	48	0.019 (−82 °C)	This work
	H$_3$PO$_4$ (100 wt% H$_3$PO$_4$)	22	2.1×10^{-4} (−82 °C)	
	H$_3$PO$_4$-0 (H$_2$O)	0.52	0.005 (−42 °C)	
	2M H$_2$SO$_4$+2M MnSO$_4$ hybrid electrolyte	531	2.66 (−70 °C)	[2]
	2M HBF$_4$+2M Mn(BF$_4$)$_2$ hybrid electrolyte	10	0.21 (−70 °C)	[3]
	H$_3$PO$_4$/MeCN	0.5	N/A	[4]
	[dema][TfO]	10	N/A	[5]
	EMImsHFd$_{2.3}$F	10	N/A	[6]
Nafion	Nafion™ 112 fully soaked in water	10	N/A	[7]
	Nafion™ 112 fully soaked in water	9	N/A	[8]
	Nafion™ 112 fully soaked in water	70	N/A	[9]
	Nafion™ 117 at 100% RH	31	N/A	[10]
	Nafion™ 117 at 100% RH	22	N/A	[11]
	Nafion™ 117 fully soaked in water	105	N/A	[12]
	Nafion™ 212 at 80% RH	38	N/A	[13]
	Nafion™ 212 at 95% RH	42	N/A	[14]
	Nafion™ 212 fully soaked in water	90	N/A	[15]
Heteropoly acid	H$_4$[In(H$_2$O)PW$_9$Mo$_2$O$_{39}$]·11H$_2$O at 80% RH	0.23	N/A	[16]
	H$_5$SiMo$_{11}$VO$_{40}$·8H$_2$O at 70% RH	5.7	N/A	[17]
	H$_6$P$_2$W$_{16}$Mo$_2$O$_{40}$·29H$_2$O at 80% RH	2.3	N/A	[18]
Layered hydrate	HUO$_2$PO$_4$·4H$_2$O in acid solution	5	N/A	[19]
	α-Zr(HPO$_4$)$_2$·nH$_2$O at 90% RH	0.001~0.01	N/A	[20]
	γ-Zr(PO$_4$)(H$_3$PO$_4$)·2H$_2$O at 90% RH	0.02	N/A	[21]
	γ-Zr sulfo phosophonates at 90% RH	10	N/A	[22]
	Layered polyvalent (Zr or Ta) hydrogen phosphate at 60% RH	0.2	N/A	[23]
MOF/COF	[Zn$_3$(H$_2$PO$_4$)$_6$(H$_2$O)$_3$](1,2,3-benzotriazole)	3.3×10^{-4}	N/A	[24]
	FeC$_2$O$_4$·2H$_2$O at 98% RH	1.3	N/A	[25]
	(NH$_4$)$_4$[MnCr$_2$(ox)$_6$]$_3$·4H$_2$O at 96% RH	1.1	N/A	[26]
	Cucurbit[6]uril(CB[6]) at 98% RH	1.1	N/A	[27]
	In-IA-2D-1 at 98% RH	3.4	N/A	[28]
	Ca-BTC-H$_2$O at 98% RH	0.12	N/A	[29]
	UiO-66 at 97% RH	7.5×10^{-3}	N/A	[30]
	MFM-510 at 99% RH	2.1×10^{-2}	N/A	[31]
	[Cr$_4$In$_4$(Himdc)$_{12}$]·H$_2$O at 98% RH	58	N/A	[32]
	Li-HPAA at 98% RH	0.11	N/A	[33]
	NH(prol)$_3$[MCr(ox)$_3$] at 75% RH	0.1	N/A	[34]

	Ca-PiPhtA-I at 98% RH	1.3	N/A	[35]
	MFM-500(Ni) at 98% RH	0.45	N/A	[36]
	MFM-500(Co) at 98% RH	4.4×10^{-2}	N/A	[36]
	MIL-100-Cr-Cl at 99.9% RH	1.6×10^{-2}	N/A	[37]
	MIL-100-Fe-Cl at 99.9% RH	6.0×10^{-2}	N/A	[37]
	MOF-801 at 98% RH	1.9	N/A	[38]
	$(H_2C_2)_2$(dtoa)Cu at 100% RH	0.1	N/A	[39]
	$[Zn(1-L_{Cl})(Cl)](H_2O)_2$ at 98% RH	0.044	N/A	[40]
	PCMOF-3 at 98% RH	0.035	N/A	[41]
	$[MIL-52(Fe)-(COOH)_2]$ at 95% RH	0.002	N/A	[42]
Modified PBI	Polybenzimidazole (PBI) at 100% RH	0.8	N/A	[43]
	Sulfonated-PBI at 100% RH	10	N/A	[44]
	PBI/HCl (11.8 M)	1.4	N/A	
	PBI/HClO$_4$ (11.6 M)	1.6	N/A	
	PBI/HNO$_3$ (15.8 M)	1.8	N/A	[45]
	PBI/H$_3$PO$_4$ (14.4 M)	1.9	N/A	
	PBI/H$_2$SO$_4$ (16 M)	60	N/A	
Modified polymer	Paam·2.4H$_3$PO$_4$	11	N/A	[46]
	PVA·H$_3$PO$_4$	98	N/A	[47]
	PEO·0.42H$_3$PO$_4$	0.03	N/A	
	PVA·0.26H$_3$PO$_4$	0.01	N/A	[48]
	PVP·2H$_3$PO$_4$	0.003	N/A	
	P2VP·2H$_3$PO$_4$	0.1	N/A	
	Nylon 6-10·2H$_3$PO$_4$	0.1~1	N/A	[49]
	GA crosslinked PVA/ 4 M H$_2$SO$_4$	600	N/A	[50]
	GA crosslinked PVA/ 2 M HClO$_4$	1	N/A	[51]
	GA crosslinked PVA/ 1.5 M HClO$_4$	1~10	N/A	[52]
	Cellulose/chitin blend/ 4 M H$_2$SO$_4$	578	N/A	[53]
	PPA blend PAAM/ 3.7 M H$_2$SO$_4$	690	N/A	[54]
	PAAK/ 1 M H$_2$SO$_4$	18	N/A	[55]
Modified HPA	H$_4$SiW$_{12}$O$_{40}$-PVA	10	N/A	[56]
	H$_4$SiW$_{12}$O$_{40}$·nH$_2$O-PWA-PVA	13	N/A	[57]
	H$_4$SiW$_{12}$O$_{40}$·H$_3$PO$_4$-PVA	8	N/A	[58]
	H$_4$SiW$_{12}$O$_{40}$·H$_3$PO$_4$-PVA	10	N/A	[59]
	Cross-linked H$_4$SiW$_{12}$O$_{40}$·H$_3$PO$_4$-PVA	15	N/A	[60]
	H$_3$PW$_{12}$O$_{40}$-C$_2$H$_7$O$_3$NS/SBA-15	50	0.07 (–40 °C)	[61]

Table S2 Synthesis parameters of AiCEs with the composition of *XY-R-N*, in which *X* (=S, H or B) refers to the type of clay (S for sepiolite, H for halloysite, B for bentonite); *Y* (=P or S) refers to the type of acid (P for phosphoric acid, S for sulfuric acid); *R* is the molar ratio of acid molecules to water*; *N* is the weight ratio of the liquid (the acid solution) to solid (clay powder).

Materials	Phyllosilicate type	Acid type	Phyllosilicate weight (mg)	Acid amount (mg)	H_2O amount (mg)	*R* ratio	*N* ratio
SP-0-3	Sepiolite	Phosphoric acid	1000	0	2758	0	3
SP-0.1-4	Sepiolite	Phosphoric acid	1000	1344	3073	0.1	4
SP-0.2-4	Sepiolite	Phosphoric acid	1000	2691	1656	0.2	4
SP-0.3-3	Sepiolite	Phosphoric acid	1000	2431	902	0.3	3
SP-0.3-4	Sepiolite	Phosphoric acid	1000	3311	1182	0.3	4
SP-0.3-5	Sepiolite	Phosphoric acid	1000	3756	1182	0.3	5
SP-0.6-4	Sepiolite	Phosphoric acid	1000	3931	551	0.5	4
SP-1.0-5	Sepiolite	Phosphoric acid	1000	4656	0	1.0	5
BP-0-1	Bentonite	Phosphoric acid	1000	0	1182	0	1
BP-0.2-1	Bentonite	Phosphoric acid	1000	744	267	0.3	1
HP-0-1	Halloysite	Phosphoric acid	1000	0	502	0	1
HP-0.3-2	Halloysite	Phosphoric acid	1000	1240	444	0.3	2
SS-0-3	Sepiolite	Sulfuric acid	1000	0	2758	0	3
SS-0.1-4	Sepiolite	Sulfuric acid	1000	984	2660	0.1	4
BS-0-1	Bentonite	Sulfuric acid	1000	0	1182	0	1
BS-0.1-1	Bentonite	Sulfuric acid	1000	311	840	0.1	1
HS-0-1	Halloysite	Sulfuric acid	1000	0	502	0	1
HS-0.1-1	Halloysite	Sulfuric acid	1000	167	449	0.1	1

*The amount of the phosphoric acid is calculated to 100% H_3PO_4 compound, which is derived from 85 wt% concentrated H_3PO_4 solution; meanwhile, the amount of H_2O is composed of two parts: the H_2O in 85 wt% concentrated H_3PO_4 solution, external added H_2O. The amount of the sulfuric acid is calculated to 100% H_2SO_4 compound, which is derived from 95 wt% concentrated H_2SO_4 solution; the amount of H_2O is composed of two parts: the H_2O in 95 wt% concentrated H_2SO_4 solution, external added H_2O.

Table S3 Composition of H_3PO_4 and H_2SO_4 with different concentrations.

Materials	Acid type	Acid amount (mg)	H_2O amount (mg)	*R* ratio
H_3PO_4-0	Phosphoric acid	0	1000	0
H_3PO_4-0.01	Phosphoric acid	69	931	0.01
H_3PO_4-0.1	Phosphoric acid	319	681	0.1
H_3PO_4-0.2	Phosphoric acid	619	381	0.2
H_3PO_4-0.3	Phosphoric acid	737	263	0.3
H_3PO_4-0.5	Phosphoric acid	882	118	0.5
H_3PO_4-1.0	Phosphoric acid	1000	0	1.0
H_3PO_4	Phosphoric acid	1000*	0	Max
H_2SO_4-0.1	Sulfuric acid	271	729	0.1

* Orthophosphoric acid crystalline was used instead of 85 wt% H_3PO_4 solution and the sample was prepared in the glovebox to avoid reaction with moisture.

Table S4 Comparison of activation energies among AiCEs, liquid proton electrolyte, other common proton electrolytes, as well as common Li-ion solid electrolytes.

Application	Materials	Temperature (°C)	Activation energy (eV) with R^2	References
Proton conductors	SP-0.3-4	25 to −16	0.12 (R^2=0.986)	This work
		−36 to −55	0.35 (R^2=0.997)	
		−58 to −72	0.46 (R^2=0.998)	
		−72 to −87	0.65 (R^2=0.999)	
		−97 to −108	0.91 (R^2=0.999)	
	HP-0.3-2	25 to −16	0.15 (R^2=0.986)	
		−29 to −49	0.31 (R^2=0.998)	
		−60 to −78	0.54 (R^2=0.999)	
		−82 to −92	0.71 (R^2=0.999)	
		−92 to −103	0.84 (R^2=0.999)	
	BP-0.2-1	25 to −16	0.22 (R^2=0.987)	
		−26 to −43	0.38 (R^2=0.998)	
		−57 to −77	0.65 (R^2=0.999)	
		−77 to −88	0.77 (R^2=0.999)	
		−88 to −99	1.00 (R^2=0.999)	
	H_3PO_4 (100 wt% H_3PO_4)	25 to −35	0.46 (R^2=0.999)	This work
		−42 to −62	0.54 (R^2=0.997)	
		−70 to −85	0.88 (R^2=0.999)	
	H_3PO_4-1.0 (85 wt% H_3PO_4)	25 to −33	0.28 (R^2=0.989)	
		−37 to −64	0.40 (R^2=0.973)	
		−64 to −80	0.68 (R^2=0.999)	
		−80 to −92	0.85 (R^2=0.999)	
	H_3PO_4-0.3 (62 wt% H_3PO_4)	25 to −16	0.19 (R^2=0.960)	
		−22 to −51	0.27 (R^2=0.990)	
		−51 to −71	0.43 (R^2=0.997)	
		−71 to −92	0.59 (R^2=0.999)	
		−92 to −104	0.82 (R^2=0.997)	
	6 wt% H_3PO_4 (H_3PO_4-0.01)	25 to −17	0.13 (R^2=0.973)	
		−17 to −30	0.90 (R^2=0.924)	
		−36 to −76	0.49 (R^2=0.996)	
		−82 to −100	0.89 (R^2=0.998)	
	H_3PO_4-0 (H_2O)	25 to −11	0.14 (R^2=0.990)	
		−11 to −17	0.73 (R^2=0.999)	
		−17 to −42	0.28 (R^2=0.993)	
	Nafion	25	0.2	[62]
	Perovskite-type	300	0.4~0.9	[63]
	Perovskite-type	400 to 700	0.3~0.5	[64]
Li-ion conductors	Sulfide-type	25	0.3~0.5	[65]
	Garnet-type		0.4~0.6	
	Anti-perovskite-type		0.2	
	NASICON type		0.3~0.5	

LISICON type		0.4~0.6
Thio-LISICON	S17	0.5~0.6
Sulfide glass		0.4~0.5
LiPON		0.45~0.55

Table S5 Rate performances and calculated energy densities for SPB.

Current density (mA g^{-1})	Specific capacity (mAh g^{-1})	Gravimetric energy density (Wh kg^{-1})	Gravimetric power density (W kg^{-1})
100	32.6	21.3	30.6
500	30.2	20.3	157.5
1000	27.5	19.1	325.9
2000	23.6	17.2	688.0
4000	19.2	14.5	1450.0
8000	15.5	10.4	2496.0
10000	14.0	8.6	2893.5
16000	10.7	5.0	3600.0

Table S6 Electrochemical comparison table considering cathode, anode, separator/thickness, voltage window, current rate range/capacity retention, lowest working temperature, and cycling capacity retention between AiCE and representative proton batteries.

Electrolyte	Cathode	Anode	Separator/ thickness	Voltage window (V)	Current rate range (A g^{-1})/ capacity retention (%) (RT)		Lowest T (°C)	Low-T capacity retention (%)	Cycling capacity retention after cycles (RT)	Refs
SP-0.3-4	**H-TBA**	**MoO₃**	**SP-0.3-4/ ~20 μm**	**1.5**	**0.05~2** **0.05~16**	**71%** **33%**	**−60**	**49%**	**74%, 20000 cycles (1 A g⁻¹)**	**This work**
62 wt% H₃PO₄	H-TBA	MoO₃	Polyethersulfone/ 100 μm	1.6	1~100	65%	−78	55%	83%, 1000 cycles (2 A g⁻¹)	[66]
1 M H₂SO₄	NiFe-TBA	AC	Whatman® Filter paper/ 180 μm	1.2	0.975~260	60%	−40	89%	73%, 1000 cycles (0.65 A g⁻¹)	[67]
0.5 M H₂SO₄	pEP(QH₂)E	pEP(NQ)E	Whatman® Glassfiber/ 200 μm	0.8	0.6~5.5	44%	−24	84%	85%, 500 cycles (0.23 A g⁻¹)	[68]
4 M H₂SO₄	PNAQ	PNAQ	N/A	1.1	1~20	90%	−70	71%	70%, 500 cycles (12 A g⁻¹)	[69]
2 M H₂SO₄	H-TBA	WO₃	Whatman® Filter paper/ 180 μm	1.5	0.0975~380	50%	25	N/A	74%, 1000 cycles (0.6 A g⁻¹)	[70]
1 M H₃PO₄/MeCN	H-TBA	MoO₃	Whatman® Filter paper/ 180 μm	1.3	0.065~0.65	70%	25	N/A	93%, 80 cycles (0.1 A g⁻¹)	[4]
0.5 M H₂SO₄	TCHQ	DCAQ	N/A	1.0	0.11~5.6	58%	25	N/A	73%, 1000 cycles (0.28 A g⁻¹)	[71]
0.05 M H₂SO₄	DPPZ	InHCF	N/A	1.3	1~10	75%	25	N/A	76%, 3000 cycles (6 A g⁻¹)	[72]
0.1 M MeTriHTFSI/ MeCN/H₂O	poly(NQ-EPE)	poly(QzH₂-EPE)	N/A	0.4	N/A	N/A	25	N/A	80%, 500 cycles (0.3 A g⁻¹)	[73]
1 M H₂SO₄	PCET	PCET	Celgard® 3401/ 20 μm	1.0	2.33~23.3	70%	25	N/A	40%, 100 cycles (2.23 A g⁻¹)	[74]

Table S7 Comparison of technical parameters of commercial Ni-Cd batteries, Ni-MH batteries, Pb-acid batteries, supercapacitors (electric double-layer capacitors), and Li-ion batteries[75].

Technical parameters	Proton batteries	Ni-Cd batteries	Ni-MH batteries	Pb-acid batteries	Supercapacitors	Li-ion batteries
Gravimetric energy density (Wh kg^{-1})	10~20	10~80	30~120	10~50	1~15	30~300
Volumetric energy density (Wh L^{-1})	20~40	15~150	40~300	25~90	1~30	200~700
Gravimetric power density (W kg^{-1})	100~10,000	150~300	700~756	75~300	1,000~60,000	230~500
Volumetric power density (W L^{-1})	200~40,000	40~700	500~3,000	10~700	4,000~120,000	100~10,000
Fast-charging time	5~60 sec	1~2 hrs	2~4 hrs	8~16 hrs	1~10 sec	0.5~4 hrs
Lifetime (cycles)	>20,000	0.3~3,000	0.3~1200	0.1~2,000	10~100,000	0.5~3,000
Cost	Low	Average	Average	Low	Low	High
Operating temperature (°C)	−60~60	−40~60	−30~60	−20~60	−40~70	−20~55
Self-discharge per day (%)	5~10	0.2~0.6	0.4~1.2	0.1~0.3	2~40	0.1~3
Overcharge tolerance/safety	High	Moderate	Low	High	High	Very low
Environmental issues	Low	High	Low	High	Moderate	Low
Commercialization since	N/A	1950	1990	1970	1975	1991

Table S8 ICP-MS analysis for the cycled liquid electrolyte in LPB.

Elements	Concentration (mmol L^{-1})	Dissolved materials (mg)	Percentage of the dissolved materials (%)
Mo	6.1±0.4	0.87 (MoO$_3$)	43.5%
Cu	2.7±0.1	0.71 (H-TBA)	17.8%
Fe	5.5±0.1	1.42 (H-TBA)	35.5%
Ti	70.5±2.6	3.37 (Ti)	46.8%

Supplementary Notes

Note S1 Illustration about NMR measurements and analysis

Initial experiments were conducted at room temperature to determine whether pulsed-field gradient diffusion experiments would be possible. 1D experiments revealed a single broad peak with a linewidth of 1.3 kHz. Estimates of T_1 and T_2 from saturation and linewidth measurements suggested T_1 (spin-lattice relaxation time) < 10 ms and T_2 (spin-spin relaxation time) <1 ms, making pulsed field gradient (PFG) diffusion coefficient measurements impossible. Thus variable temperature (from −40 °C to 80 °C in ten-degree increments, with an additional measurement taken at 25 °C) T_1 measurements, using an inversion recovery pulse sequence, were performed to access the self-diffusion coefficients indirectly.

Figure S5a illustrates a typical magnetization recovery profile, indicating single-exponential recovery. T_1 was uniformly less than 10 ms, and decreased as the temperature was increased, reaching a minimum of around 35 °C, before beginning to increase again, as displayed in **Figure S5b**, which plots the relaxation rate, $R = 1/T_1$. Based on the phenomenological model of Bloembergen, Pound, and Purcell (BPP Model)[76], the relaxation rate $R = 1/T_1$ is proportional to the spectral density function of the molecular motion $J(\omega)$, which is the fourier transform of the autocorrelation function of relative position between dipoles $K(t)$. The BPP model assumes a simple exponentially decaying autocorrelation function with the characteristic time τ_c, $K(t) \propto e^{-t/\tau_c}$. In this case, R_1 takes the form

$$R_1 = A\left(\frac{\tau_c}{1 + \omega^2\tau_c{}^2} + \frac{2\tau_c}{1 + 4\omega^2\tau_c{}^2}\right)$$

where ω is the Larmor frequency of the nucleus under observation and A is a temperature and frequency independent parameter depending only on the interaction strength between dipoles, with dimensions of s^{-2}. One of the benefits of the BPP model is it predicts the existence of R_1 maximum (T_1 minimum) at $\omega\tau_c = \frac{1}{\sqrt{2}}$, where $R_{1max} = \frac{2^{3/2}A}{3\omega}$. Using a simple quadratic fit to estimate the position and value of R_1 maximum, we found the maximum occurs at T_{max}=34.8 °C at R_1=486 Hz. Using our known proton frequency of 301.40 MHz, we calculated a correlation time of $\tau_c = 3.73 \times 10^{-10}$ s and $A = 9.76 \times 10^{11}$ Hz^2. Using this fit parameter A, we calculated correlation times from each measured R_1. Correlation times showed characteristic Arrhenius behavior, as shown in **Figure S5c**. A deviation in the slope of the Arrhenius plot can be observed around T=0 °C, indicating larger activation energy below this value. The activation apparent activation energies for correlation times measured above and below 0 °C were 0.149 eV and 0.201 eV, respectively. While there is no sudden change in dynamics that would be expected from a liquid to solid phase transition, there does appear to be a change in the nature of the dynamic process below the freezing point of water, as shown by the change in activation energy.

The monoexponential character and rapid relaxation rate suggest that proton relaxation is strongly affected by confinement in the AiCEs. We assume a predominantly diffusion mediated relaxation, with nuclear dipolar coupling influenced by molecular rotation making an insignificant contribution. Therefore, we may identify the correlation time with the mean free time in a diffusion process.

Diffusion coefficients can then be calculated from our measured correlation times using an assumed mean free path, which for a liquid we assume to be $\lambda = 2$ Å, roughly the radius of a spherical cell containing a single water molecule in the liquid state. We can then calculate $D = \frac{\lambda^2}{2n\tau_c}$, where n is the dimension of the diffusion. Our calculated diffusion coefficients range from around 2.14×10^{-12} m^2 s^{-1} at $-40\,°$C, 1.44×10^{-11} m^2 s^{-1} at 25 °C, and 3.66×10^{-11} m^2 s^{-1} at 80 °C (**Figure S5d**). While our estimate of $\lambda = 2$ Å is reasonable for small molecules and certainly the correct order of magnitude, λ could conceivably be shorter or longer than a molecular radius, and a better estimate is necessary to constrain estimates of D which varies with λ^2. We suggest that these are reasonable upper and lower bounds for the diffusion coefficient, but a better estimate of λ is required to constrain D further. Nonetheless, regardless of the model details and precise value of λ, the temperature dependence reflects an activation process that is consistent with the conductivity measurements.

Note S2 Analysis of the structural diffusion mechanism vs packed-acid mechanism

Proton transport can be remarkably fast ($10^0\sim10^3$ mS cm^{-1}) due to the unique Grotthuss mechanism[77]. In the Grotthuss mechanism, protons move along a hydrogen bond (H−bond) network via two steps: I) hopping, in which a proton hops from a proton donor to a proton acceptor along an H−bond ($-$OH$^{..}$ O$- \rightarrow -$O$^{..}$HO$-$), and II) reorientation, in which an H−bond in $-$O$^{..}$HO$-$ is cleaved, the $-$OH reorients to the O in another nearby proton acceptor and forms a new H−bond.

In acid solutions, protons exist as hydronium ions (H$_3$O$^+$). Among the two steps in the Grotthuss mechanism, reorientation of $-$OH is the rate-limiting step due to the difficulty in cleaving H−bonds, especially the H-bonds between H$_2$O and H$_3$O$^+$ [78]. H$_3$O$^+$ is surrounded by two hydration shells: the primary hydration shell and the secondary hydration shell[79],[80]. Depending on the concentration of H$_3$O$^+$, the water of a hydration shell of an H$_3$O$^+$ ion can be solely owned by that H$_3$O$^+$ ion or shared with another neighboring H$_3$O$^+$. The former typically occurs in *dilute acid*, in which H$_3$O$^+$ ions exist at further distances from one another, thereby rendering their interactions negligible. In contrast, the latter happens in *concentrated acid*, in which H$_3$O$^+$ ions exist in relatively close proximity with each other and therefore there is a strong interaction between them (called acid-acid interaction).

In *dilute acid*, due to the strong H−bond between the central H$_3$O$^+$ ion and its primary hydration shell water, reorientation of $-$OH in the water of its primary hydration shell is difficult. Therefore, Grotthuss proton transport mainly occurs via the reorientation of $-$OH in its secondary hydration shell water. This Grotthuss mechanism is called the *structural diffusion mechanism* and it relies on the thermal fluctuation of water molecules in the secondary hydration shell of H$_3$O$^+$. In *concentrated acid*, however, the H−bonds between the central H$_3$O$^+$ and its primary hydration shell water are weakened by a nearby H$_3$O$^+$. As such, the reorientation of $-$OH in the water of its primary hydration shell is much easier. This allows the Grotthuss mechanism to occur via the reorientation of $-$OH in both the primary and secondary hydration shell waters. At a very high H$_3$O$^+$ concentration, there could be another H$_3$O$^+$ ion present in the primary solvation shell of an H$_3$O$^+$ ion. In this case, proton transport can occur via the

reorientation of the −OH of the H_3O^+. Because of the close proximity of the H_3O^+ ions in concentrated acid solutions, this mechanism is referred to as the *packed-acid mechanism*[81].

Based on the discussions above, if a sharp drop in conductivity is observed when the temperature drops below the freezing temperature, the proton conduction is primarily relying on the structural diffusion mechanism. If there is no sharp drop in conductivity, the proton conduction is mainly due to the packed-acid mechanism. To obtain a clearer understanding of the differences between electrolytes that conduct via the structural diffusion mechanism vs those that conduct via the packed-acid mechanism, we prepared a dilute H_3PO_4 acid solution with R=0.01 (H_3PO_4-0.01) to compare with the concentrated acid solution with R>0.1 (*e.g.*, H_3PO_4-0.3, **Figure S3b**). For H_3PO_4-0.3, the proton conductivity is 46 mS cm^{-1} at 25 °C, and decreases gradually from 15 mS cm^{-1} at −20 °C to 10 mS cm^{-1} at −30 °C (with a corresponding increase in the activation energy from 0.19 eV to 0.27 eV). In contrast, for H_3PO_4-0.01, the proton conductivity shows 12 mS cm^{-1} at 25 °C, but it drops rapidly from 7 mS cm^{-1} at −20 °C to 0.2 mS cm^{-1} at −30 °C (with the corresponding activation energy increasing from 0.13 eV to 0.90 eV). This sharp drop could be due to the freezing of water in the structural diffusion mechanism. Therefore, compared with the ~350-fold sharp drop from −20 °C to −30 °C for the electrolytes with the structural diffusion mechanism of conduction, the ~650-fold gradual drop from 25 °C to −82 °C for the electrolytes with the packed-acid mechanism is excellent in terms of proton transport kinetics. In other words, compared with dilute acid solutions and most of the proton solid electrolytes that rely on the thermal fluctuation of water (**Figure 2a**), the proton transport kinetics for concentrated acid solutions and AiCEs is far superior, especially for environmental conditions with less humidity or low temperature. These excellent proton transport kinetics can support the operation of the proton batteries at low temperatures and is a significant advantage of the packed-acid mechanism.

Note S3 *Ex situ* X-ray photoelectron spectroscopy (XPS) analysis of the electrodes in LPB

Compared with the pristine H-TBA at the cathode (**Figure S15a**), the Cu and Fe signals of the cathodes before and after cycling were not distinct, implying a passivation layer was formed on the surface of the cathode (consistent with the relatively mild gassing phenomenon of LPB in **Figure 5a** and **Video S1**).

Note S4 Structural and conductivity analyses of H_2SO_4-based AiCEs

Like H_3PO_4-based AiCEs, when H_2SO_4 molecules are absorbed into the structure, a similar gel-like phase with low crystallinity can be obtained (**Figures S18a~c**). The proton conductivity is also enhanced up to 20 mS cm^{-1} under room temperature with the optimized composition of R=0.1, N=4 for sepiolite (SS-0.1-4), R=0.1, N=1 for bentonite (BS-0.1-1), and R=0.1, N=1 for halloysite (HS-0.1-1). The proton conductivity gradually decreases with decreasing temperatures, and 0.09 mS cm^{-1} (SS-0.1-4), 0.04 mS cm^{-1} (BS-0.1-1), and 0.03 mS cm^{-1} (HS-0.1-1) can be realized at −82 °C (**Figures S18d~f**).

Note S5 Chemical and electrochemical stability analyses of H₂SO₄-based AiCEs

The electrochemical and chemical stability window of SS-0.1-4 was investigated by linear scanning voltammetry and corrosivity measurements. As shown in **Figure S19a**, the electrochemical stability window is expanded from 1.7 V for H_2SO_4-0.1 to 2.2 V for SS-0.1-4 at the scan rate of 0.1 mV s^{-1}. The expanded potential operation range benefits the energy density of the proton batteries, as well as helps to suppress the gassing issue. Furthermore, the corrosion potential is suppressed from −525 mV for H_2SO_4-0.1 to −441 mV for SS-0.1-4 (vs Pt^{2+}/Pt) with a much lower exchange current of 0.09 μA cm^{-2} (**Figure S19b**).

Supplementary References

[1]   Y. S. Wang, Y. Alrefaei, J. G. Dai, *Front. Mater.* **2019**, 6, 1.

[2]   Z. Guo, J. Huang, X. Dong, Y. Xia, L. Yan, Z. Wang, Y. Wang, *Nat. Commun.* **2020**, 11, 959.

[3]   T. J. Sun, H. H. Du, S. B. Zheng, J. Q. Shi, Z. L. Tao, *Adv. Funct. Mater.* **2021**, 31, 2010127.

[4]   Y. Xu, X. Wu, H. Jiang, L. Tang, K. Y. Koga, C. Fang, J. Lu, X. Ji, *Angew. Chem. Int. Ed. Engl.* **2020**, 59, 22007.

[5]   S. Y. Lee, A. Ogawa, M. Kanno, H. Nakamoto, T. Yasuda, M. Watanabe, *J. Am. Chem. Soc.* **2010**, 132, 9764.

[6]   R. Hagiwara, T. Nohira, K. Matsumoto, Y. Tamba, *Electrochem. Solid-State Lett.* **2005**, 8, 231.

[7]   L. Merlo, A. Ghielmi, L. Cirillo, M. Gebert, V. Arcella, *Sep. Sci. Technol.* **2007**, 42, 2891.

[8]   F. Pereira, K. Valle, P. Belleville, A. Morin, S. Lambert, C. Sanchez, *Chem. Mater.* **2008**, 20, 1710.

[9]   J. Peron, A. Mani, X. Zhao, D. Edwards, M. Adachi, T. Soboleva, Z. Shi, Z. Xie, T. Navessin, S. Holdcroft, *J. Membr. Sci.* **2010**, 356, 44.

[10]   H. Wang, B. A. Holmberg, L. Huang, Z. Wang, A. Mitra, J. M. Norbeck, Y. Yan, *J. Mater. Chem.* **2002**, 12, 834.

[11]   H. Ahmad, S. K. Kamarudin, U. A. Hasran, W. R. W. Daud, *Int. J. Hydrogen Energy* **2011**, 36, 14668.

[12]   Y. Yin, J. Fang, Y. Cui, K. Tanaka, H. Kita, K.-i. Okamoto, *Polymer* **2003**, 44, 4509.

[13]   J. Choi, K. M. Lee, R. Wycisk, P. N. Pintauro, P. T. Mather, *J. Electrochem. Soc.* **2010**, 157.

[14]   H.-Y. Li, Y.-L. Liu, *J. Mater. Chem. A* **2014**, 2, 3783.

[15]   J. Li, K. Fan, W. Cai, L. Ma, G. Xu, S. Xu, L. Ma, H. Cheng, *J. Power Sources* **2016**, 332, 37.

[16]   X. Wu, Q. Wu, *Dalton Trans.* **2021**, 50, 6793.

[17]   Z. Xie, H. Wu, Q. Wu, L. Ai, *RSC Adv.* **2018**, 8, 13984.

[18]   X. Wu, Q. Wu, *Funct. Mater. Lett.* **2021**, 2150019.

[19]   A. T. Howe, M. G. Shilton, *J. Solid State Chem.* **1979**, 28, 345.

[20]   G. Alberti, M. Casciola, *Solid State Ion.* **1997**, 97, 177.

[21]   G. Alberti, M. Casciola, L. Massinelli, R. Palombari, *Ionics* **1996**, 2, 179.

[22]   G. Alberti, L. Boccali, M. Casciola, L. Massinelli, E. Montoneri, *Solid State Ion.* **1996**, 84, 97.

[23]   V. A. Tarnopolsky, I. A. Stenina, A. B. Yaroslavtsev, *Solid State Ion.* **2001**, 145, 261.

[24]   N. Ma, S. Kosasang, A. Yoshida, S. Horike, *Chem. Sci.* **2021**, 12, 5818.

[25]   S. Chandra, T. Kundu, S. Kandambeth, R. Babarao, Y. Marathe, S. M. Kunjir, R. Banerjee, *J. Am. Chem. Soc.* **2014**, 136, 6570.

[26]   E. Pardo, C. Train, G. Gontard, K. Boubekeur, O. Fabelo, H. Liu, B. Dkhil, F. Lloret, K. Nakagawa, H. Tokoro, S. Ohkoshi, M. Verdaguer, *J. Am. Chem. Soc.* **2011**, 133, 15328.

[27]   M. Yoon, K. Suh, H. Kim, Y. Kim, N. Selvapalam, K. Kim, *Angew. Chem. Int. Ed. Engl.* **2011**, 50, 7870.

[28]   T. Panda, T. Kundu, R. Banerjee, *Chem. Commun.* **2013**, 49, 6197.

[29]   A. Mallick, T. Kundu, R. Banerjee, *Chem. Commun.* **2012**, 48, 8829.

[30]   F. Yang, H. Huang, X. Wang, F. Li, Y. Gong, C. Zhong, J.-R. Li, *Crystal Growth & Design* **2015**, 15, 5827.

[31]   P. Rought, C. Marsh, S. Pili, I. P. Silverwood, V. G. Sakai, M. Li, M. S. Brown, S. P. Argent, I. Vitorica-Yrezabal, G. Whitehead, *Chem. Sci.* **2019**, 10, 1492.

[32] Q. G. Zhai, C. Mao, X. Zhao, Q. Lin, F. Bu, X. Chen, X. Bu, P. Feng, *Angew. Chem.* **2015**, 127, 7997.

[33] M. Bazaga-García, M. Papadaki, R. M. Colodrero, P. Olivera-Pastor, E. R. Losilla, B. n. Nieto-Ortega, M. A. n. G. Aranda, D. Choquesillo-Lazarte, A. Cabeza, K. D. Demadis, *Chem. Mater.* **2015**, 27, 424.

[34] H. Okawa, A. Shigematsu, M. Sadakiyo, T. Miyagawa, K. Yoneda, M. Ohba, H. Kitagawa, *J. Am. Chem. Soc.* **2009**, 131, 13516.

[35] M. Bazaga-Garcia, R. M. Colodrero, M. Papadaki, P. Garczarek, J. Zon, P. Olivera-Pastor, E. R. Losilla, L. Leon-Reina, M. A. Aranda, D. Choquesillo-Lazarte, *J. Am. Chem. Soc.* **2014**, 136, 5731.

[36] S. Pili, S. P. Argent, C. G. Morris, P. Rought, V. García-Sakai, I. P. Silverwood, T. L. Easun, M. Li, M. R. Warren, C. A. Murray, *J. Am. Chem. Soc.* **2016**, 138, 6352.

[37] C. Mao, R. A. Kudla, F. Zuo, X. Zhao, L. J. Mueller, X. Bu, P. Feng, *J. Am. Chem. Soc.* **2014**, 136, 7579.

[38] J. Zhang, H.-J. Bai, Q. Ren, H.-B. Luo, X.-M. Ren, Z.-F. Tian, S. Lu, *ACS Appl. Mater. Interfaces* **2018**, 10, 28656.

[39] T. Yamada, S. Morikawa, H. Kitagawa, *Bull. Chem. Soc. Jpn.* **2010**, 83, 42.

[40] S. C. Sahoo, T. Kundu, R. Banerjee, *J. Am. Chem. Soc.* **2011**, 133, 17950.

[41] J. M. Taylor, R. K. Mah, I. L. Moudrakovski, C. I. Ratcliffe, R. Vaidhyanathan, G. K. Shimizu, *J. Am. Chem. Soc.* **2010**, 132, 14055.

[42] A. Shigematsu, T. Yamada, H. Kitagawa, *J. Am. Chem. Soc.* **2011**, 133, 2034.

[43] D. Hoel, E. Grunwald, *J. Phys. Chem.* **1977**, 81, 2135.

[44] X. Glipa, M. ElHaddad, D. J. Jones, J. Roziere, *Solid State Ion.* **1997**, 97, 323.

[45] D. J. Jones, J. Roziere, *J. Membr. Sci.* **2001**, 185, 41.

[46] D. Rodriguez, C. Jegat, O. Trinquet, J. Grondin, J. Lassegues, *Solid State Ion.* **1993**, 61, 195.

[47] V. Vijayakumar, M. Ghosh, A. Torris A. T, N. C. M. K, S. B. Nair, M. V. Badiger, S. Kurungot, *ACS Sustain. Chem. Eng.* **2018**, 6, 12630.

[48] P. Kölsch, *Z. Phys. Chem.* **1994**, 184, 297.

[49] J. Grondin, D. Rodriguez, J. C. Lassègues, *Solid State Ion.* **1995**, 77, 70.

[50] S. Nohara, T. Miura, C. Iwakura, H. Inoue, *Electrochemistry* **2007**, 75, 579.

[51] S. Sampath, N. A. Choudhury, A. K. Shukla, *J. Chem. Sci.* **2009**, 121, 727.

[52] N. A. Choudhury, A. K. Shukla, S. Sampath, S. Pitchumani, *J. Electrochem. Soc.* **2006**, 153.

[53] S. Yamazaki, A. Takegawa, Y. Kaneko, J.-i. Kadokawa, M. Yamagata, M. Ishikawa, *Electrochem. Commun.* **2009**, 11, 68.

[54] I. Stepniak, A. Ciszewski, *Electrochim. Acta* **2011**, 56, 2477.

[55] K. M. Kim, J. H. Nam, Y.-G. Lee, W. I. Cho, J. M. Ko, *Curr. Appl. Phys.* **2013**, 13, 1702.

[56] K. Lian, C. M. Li, *Electrochem. Commun.* **2009**, 11, 22.

[57] H. Gao, K. Lian, *Electrochim. Acta* **2010**, 56, 122.

[58] H. Gao, K. Lian, *J. Power Sources* **2011**, 196, 8855.

[59] H. Gao, K. Lian, *J. Electrochem. Soc.* **2011**, 158.

[60] H. Gao, K. Lian, *J. Mater. Chem.* **2012**, 22.

[61] X. Sun, S. Liu, S. Zhang, T. Dang, H. Tian, Y. Lu, S. Liu, *ACS Appl. Energy Mater.* **2020**, 3, 1242.

[62] F. C. Teixeira, A. I. de Sá, A. P. S. Teixeira, C. M. Rangel, *Appl. Surf. Sci.* **2019**, 487, 889.

[63]   Y. Meng, J. Gao, Z. Zhao, J. Amoroso, J. Tong, K. S. Brinkman, *J. Mater. Sci.* **2019**, 54, 9291.

[64]   a) Y. Zhou, X. Guan, H. Zhou, K. Ramadoss, S. Adam, H. Liu, S. Lee, J. Shi, M. Tsuchiya, D. D. Fong, S. Ramanathan, *Nature* **2016**, 534, 231; b) D. A. Medvedev, J. G. Lyagaeva, E. V. Gorbova, A. K. Demin, P. Tsiakaras, *Prog. Mater Sci.* **2016**, 75, 38.

[65]   a) P. Knauth, *Solid State Ion.* **2009**, 180, 911; b) Y. Chen, K. Wen, T. Chen, X. Zhang, M. Armand, S. Chen, *Energy Storage Mater.* **2020**, 31, 401.

[66]   H. Jiang, W. Shin, L. Ma, J. J. Hong, Z. X. Wei, Y. S. Liu, S. Y. Zhang, X. Y. Wu, Y. K. Xu, Q. B. Guo, M. A. Subramanian, W. F. Stickle, T. P. Wu, J. Lu, X. L. Ji, *Adv. Energy Mater.* **2020**, 10, 2000968.

[67]   X. Wu, S. Qiu, Y. Xu, L. Ma, X. Bi, Y. Yuan, T. Wu, R. Shahbazian-Yassar, J. Lu, X. Ji, *ACS Appl. Mater. Interfaces* **2020**, 12, 9201.

[68]   C. Strietzel, M. Sterby, H. Huang, M. Stromme, R. Emanuelsson, M. Sjodin, *Angew. Chem. Int. Ed. Engl.* **2020**, 59, 9631.

[69]   T. Sun, H. Du, S. Zheng, J. Shi, X. Yuan, L. Li, Z. Tao, *Small Methods* **2021**, DOI: 10.1002/smtd.202100367.

[70]   X. Y. Wu, J. J. Hong, W. Shin, L. Ma, T. C. Liu, X. X. Bi, Y. F. Yuan, Y. T. Qi, T. W. Surta, W. X. Huang, J. Neuefeind, T. P. Wu, P. A. Greaney, J. Lu, X. L. Ji, *Nat. Energy* **2019**, 4, 123.

[71]   T. Tomai, S. Mitani, D. Komatsu, Y. Kawaguchi, I. Honma, *Sci. Rep.* **2014**, 4, 3591.

[72]   J. Qiao, M. Qin, Y. M. Shen, J. Cao, Z. Chen, J. Xu, *Chem. Commun. (Camb)* **2021**, 57, 4307.

[73]   H. Wang, R. Emanuelsson, C. Karlsson, P. Jannasch, M. Stromme, M. Sjodin, *ACS Appl. Mater. Interfaces* **2021**, 13, 19099.

[74]   L. Tong, Y. Jing, R. G. Gordon, M. J. Aziz, *ACS Appl. Energy Mater.* **2019**, 2, 4016.

[75]   a) A. Alhamali, M. E. Farrag, G. Bevan, D. M. Hepburn, presented at 2016 Eighteenth International Middle East Power Systems Conference (MEPCON) **2016**; b) X. Fan, B. Liu, J. Liu, J. Ding, X. Han, Y. Deng, X. Lv, Y. Xie, B. Chen, W. Hu, C. Zhong, *Trans. Tianjin Univ.* **2020**, 26, 92; c) M. M. Rahman, A. O. Oni, E. Gemechu, A. Kumar, *Energy Convers. Manage.* **2020**, 223; d) G. J. May, A. Davidson, B. Monahov, *J. Energy Storage* **2018**, 15, 145; e) A. G. Olabi, C. Onumaegbu, T. Wilberforce, M. Ramadan, M. A. Abdelkareem, A. H. Al – Alami, *Energy* **2021**, 214; f) S. Koohi-Fayegh, M. A. Rosen, *J. Energy Storage* **2020**, 27, 101047.

[76]   N. Bloembergen, E. M. Purcell, R. V. Pound, *Phys. Rev.* **1948**, 73, 679.

[77]   N. Agmon, *Chem. Phys. Lett.* **1995**, 244, 456.

[78]   T. Ogawa, T. Aonuma, T. Tamaki, H. Ohashi, H. Ushiyama, K. Yamashita, T. Yamaguchi, *Chem. Sci.* **2014**, 5, 4878.

[79]   A. Rahmouni, E. Kochanski, R. Wiest, P. E. S. Wormer, J. Langlet, *J. Chem. Phys.* **1990**, 93, 6648.

[80]   E. Kochanski, *J. Am. Chem. Soc.* **1985**, 107, 7869.

[81]   T. Ogawa, H. Ohashi, T. Tamaki, T. Yamaguchi, *Chem. Phys. Lett.* **2019**, 731, 136627.